

1
2 **Scaling laws for mixed-heated stagnant-lid convection**
3 **and application to Europa**
4
5

6
7 Frédéric Deschamps¹ and Kenny Vilella²
8

9 ¹ Institute of Earth Sciences, Academia Sinica, 128 Academia Road Sec. 2, Nangang, Taipei
10 11529, Taiwan.

11 ² JSPS International Research Fellow, Hokkaido University, Sapporo, Japan.
12
13

14 Corresponding author: Frédéric Deschamps; email: frederic@earth.sinica.edu.tw
15
16
17

18 Submitted to *Journal of Geophysical Research Planets*
19 May 24th 2021, 42 pages, including 3 tables and 8 figures
20
21
22
23
24

25 **Abstract.** Because rocks and ices viscosities strongly depend on temperature, planetary
26 mantles and ice shells are often thought to be animated by stagnant-lid convection. Their
27 dynamics is further impacted by the release of internal heat either through radioactive isotopes
28 decay or tidal dissipation. Here, we quantify the impact of internal heating on stagnant-lid
29 convection. We performed numerical simulations of convection combining strongly
30 temperature-dependent viscosity and mixed (basal and internal) heating in 3D-Cartesian and
31 spherical geometries, and used these simulations to build scaling laws relating surface heat flux,
32 Φ_{surf} , interior temperature, T_m , and stagnant lid thickness, d_{lid} , to the system Rayleigh number,
33 heating rate, H , and top-to-bottom viscosity ratio, $\Delta\eta$. These relationships show that T_m
34 increases with H but decreases with $\Delta\eta$, while Φ_{surf} increases with H and $\Delta\eta$. Importantly, they
35 also describe heterogeneously heated systems well, provided that the maximum dissipation
36 occurs in hottest regions. For H larger than a critical value H_{crit} , the bottom heat flux turns
37 negative and the system cools down both at its top and bottom. Two additional interesting
38 results are that 1) while the rigid lid stiffens with increasing H , it also thins; and 2) H_{crit} increases
39 with increasing $\Delta\eta$. We then use our scaling laws to assess the impact of tidal heating on
40 Europa's ice shell properties and evolution. Our calculations suggest a shell thickness in the
41 range 20-80 km, depending on viscosity and dissipated power, and show that internal heating
42 has a stronger influence than the presence of impurities in the sub-surface ocean.
43

44
45
46
47
48
49
50
51
52
53
54
55
56
57
58
59
60
61
62
63
64
65
66
67
68

Plain language summary. Convection is a mode of heat transfer that is thought to play or have played a key role in the cooling of planetary mantles and ice shells of icy bodies. The convection vigor, efficiency and ability to transport heat are all controlled by the properties of the systems in which it settles. In planetary mantles and ice shells, two important parameters are the variations of viscosity triggered by changes in temperature, which lead to the formation of a rigid lid at the top of the system, and the production of heat within the system, which weakens hot plumes rising from its base. In this article, we assess the combined effects of these two parameters. For this, we perform numerical simulations of convection, from which we deduce quantitative relationships between input and output parameters, the later including internal temperature and surface heat flux. We show that both heat flux and temperature increase with increasing internal heat production, while increasing the thermal viscosity contrast increases heat flux, but reduces temperature. We then apply our relationships to the case of Europa, a moon of Jupiter, and show that the thickness of its ice shell should be in the range 20-80 km.

Key points.

- We run simulations of stagnant-lid mixed-heated convection and build temperature and heat flux scaling laws from them
- Stagnant lid stiffens and thins with increasing rate of internal heating
- The critical rate of internal heating at which bottom heat flux turns negative increases with increasing viscosity ratio

69 1. Introduction

70 Heat transfer through planetary mantles and ice shells of large icy bodies is controlled by the
71 properties of these systems. Due to the strong temperature-dependence of silicate rocks and ices
72 viscosities, convection within these systems is likely to operate in the so-called stagnant-lid
73 regime (*e.g.*, Christensen, 1984; Moresi and Solomatov, 1995), unless, as in the case of the
74 Earth, specific conditions allow the development of plate tectonics. In stagnant-lid convection,
75 a rigid layer forms at the top of the system as an extension of the top thermal boundary layer
76 (TBL). Because this layer is not mobile and transports heat by conduction, its presence strongly
77 alters heat transfer through the system. Another process altering the ability of convection to
78 transfer heat towards the surface is the production of heat within the system. In systems heated
79 both from their bases and their interiors, hot plumes rising from the bottom TBL get weaker
80 with increasing rate of internal heating, and may not reach the surface if heat production is too
81 high (*e.g.*, Travis and Olson, 1994; Deschamps et al., 2010a). As a result, the amount of heat
82 that can be extracted from regions located beneath the system is reduced. Ultimately, for
83 internal heating rate larger than a critical value, the bottom heat flux turns negative, meaning
84 that the system cools down both from its top and its base. In rocky planets, a source of internal
85 heating is the decay of long-lived radio elements (^{235}U , ^{238}U , ^{232}Th , and ^{40}K). Short-lived
86 elements, mainly ^{26}Al , may have further played a role in the evolution of planetesimals, the
87 parent bodies of rocky planets and asteroids. In the case of icy moons, tidal dissipation provides
88 a source of heat within or at the bottom of the ice shell. The amount of heat released, and thus
89 the evolution of the body, depends on its orbital properties and may vary with time (*e.g.*, Tobie
90 et al., 2003, 2005; Roberts and Nimmo, 2008), with internal heating being null or negligible if
91 the body is tidally locked or if it moves on a quasi-circular orbit. Quantifying the influence of
92 internal heating on the ability of rocky mantles and ice shells to transport heat towards the

93 surface is therefore essential to model accurately the long term evolution of icy bodies and
 94 rocky planets.

95 A convenient way to quantify these effects is to build relationships (or scaling laws)
 96 between the key parameters describing thermal evolution (mainly interior temperature and
 97 surface heat flux) and the system properties, for instance its rheology, Rayleigh number (which
 98 measures the vigor of convection and depends itself on the system physical and thermal
 99 properties), and rate of internal heating. Scaling laws may be built from series of numerical
 100 simulations of convection, in which one or more parameters are systematically varied. Here,
 101 we conduct such a study in the case of mixed-heated systems animated by stagnant-lid
 102 convection. In addition to building scaling laws, we parameterize the value of internal heating
 103 at which the bottom heat flux turns negative. Finally, we use our results to model the properties
 104 and evolution of Europa's outer ice shell.

105

106 2. Numerical model and simulations

107 We performed numerical simulations of thermal convection for an incompressible, infinite
 108 Prandtl number fluid using StagYY (Tackley, 2008). The fluid is heated both from the bottom
 109 and from within, and the internal heating is controlled by the heat production per unit of mass,
 110 H . The conservation equations of momentum, mass, and energy are then

$$111 \quad \nabla \bar{\sigma} - \nabla P = -\alpha \rho g T \mathbf{e}_z \quad (1)$$

$$112 \quad \nabla \cdot \mathbf{v} = 0 \quad (2)$$

$$113 \quad \text{and } \rho C_P \frac{\partial T}{\partial t} = k \nabla \cdot (\nabla T) - \rho C_P \mathbf{v} \cdot \nabla T + \rho H, \quad (3)$$

114 where the elements of the deviatoric stress tensor, $\bar{\sigma}$, are $\sigma_{ij} = \eta(\partial v_i / x_j + \partial v_j / x_i)$, P is the
 115 non-hydrostatic pressure, \mathbf{v} the velocity, T the temperature, \mathbf{e}_z the radial unit vector, α , ρ , and
 116 C_P , and k the fluid thermal expansion, density, heat capacity and thermal conductivity (all

117 assumed constant throughout the system), g the gravity acceleration, and η the fluid viscosity,
 118 which here varies with temperature. Numerical methods used to solve Eqs. (1) to (3) are detailed
 119 in Tackley (2008).

120 The geometry is either 3D-Cartesian or 3D-spherical. In this later case, the spherical shell
 121 is modelled with a set of Yin and Yang stripes (Kageyama and Sato, 2004), the shell curvature
 122 being controlled by the ratio between its inner and outer radii, $f = r_c/R$. Depending on the
 123 curvature and on the effective Rayleigh number, Ra_{eff} (defined below), the resolution of each
 124 Yin or Yang stripe varies between 192×576 and 512×1536 (corresponding to spherical grids of
 125 384×768 to 1024×2048 points), and the radial resolution of the shell varies between 96 and 192
 126 points. 3D-Cartesian simulations are performed in boxes with a horizontal to vertical aspect
 127 ratio equal to 4 in both x and y directions, and a grid resolution of $128 \times 128 \times 64$ points for Ra_{eff}
 128 $< 10^6$, $256 \times 256 \times 128$ points for $10^6 \leq Ra_{\text{eff}} < 10^8$, and $384 \times 384 \times 192$ points for $Ra_{\text{eff}} \geq 10^8$. In
 129 addition, for both 3D-Cartesian and 3D-spherical cases, the grid is vertically refined at the top
 130 and at the bottom of the domain. Overall, this provides a good sampling of plumes and thermal
 131 boundary layers, when they exist. The top and bottom boundaries are free slip and isothermal,
 132 and reflective boundary conditions are imposed on sidewalls of 3D-Cartesian simulations. In
 133 all cases, initial temperature distributions are built from random perturbations superposed on a
 134 1D radial adiabatic profile with thin TBLs at top and bottom.

135 Conservation equations are non-dimensionalized with the characteristic properties of the
 136 system. Hereafter, non-dimensional quantities are distinguished from their dimensional forms
 137 by adding a tilde, \sim . We used the thickness of the fluid layer, D , as characteristic length, and
 138 the super-adiabatic temperature jump across this layer, ΔT , as characteristic temperature. The
 139 non-dimensional temperature and internal heating rate are then given by $\tilde{T} = (T - T_{\text{surf}})/\Delta T$,
 140 where T_{surf} is the surface temperature, and

$$141 \quad \tilde{H} = \frac{\rho H D^2}{\kappa \Delta T}. \quad (4)$$

142 Non-dimensionalization further implies to replace the source term of momentum equation,
 143 $\alpha\rho gT$, by the Rayleigh number,

$$144 \quad Ra = \frac{\alpha\rho g\Delta TD^3}{\eta\kappa}, \quad (5)$$

145 where $\kappa = k/\rho C_p$ is the thermal diffusivity. This number measures the ratio between buoyancy
 146 and viscous forces, and is an input parameter of our simulations.

147 The viscosity of ice strongly depends on temperature. Here, we modelled this dependency
 148 using the Frank-Kamenetskii (FK) approximation,

$$149 \quad \eta = \eta_0 \exp\left[-a_\eta \frac{(T-T_0)}{\Delta T}\right], \quad (6)$$

150 where η_0 and T_0 are the reference viscosity and temperature, and a_η a parameter that controls
 151 the amplitude of viscosity variations. This approximation overestimates the surface heat flux
 152 by up to 30 % (*e.g.*, Reese et al., 1999), and it does not account for dependencies of viscosity
 153 on strain rate and grain size. Nevertheless, it facilitates the calculations and allows capturing
 154 the role of one specific parameter (here, internal heating), since a large number of FK
 155 simulations are available in the literature and can be used for comparisons. In the FK
 156 approximation, the non-dimensional viscosity, $\tilde{\eta} = \eta/\eta_0$, is given as a function of the non-
 157 dimensional temperature, \tilde{T} , by

$$158 \quad \tilde{\eta} = \exp(-a_\eta \tilde{T}). \quad (7)$$

159 The top-to-bottom viscosity ratio, $\Delta\eta = \exp(a_\eta)$, is an input parameter of our simulations. For
 160 viscosity ratios larger than 10^4 , convection generally operates in the so-called stagnant-lid
 161 regime (*e.g.*, Christensen, 1984; Davaille and Jaupart, 1993; Moresi and Solomatov, 1995), in
 162 which a highly viscous (stagnant) lid develops at the top of the fluid. In this layer, heat is
 163 transported by conduction, thus reducing the heat transfer. Experimental rheological laws for
 164 ice Ih (Durham et al., 2010) imply that the top-to-bottom viscosity ratios through the outer ice

165 shells of icy bodies are much larger than 10^4 . Convection within these shells, if occurring, should
 166 then operate in the stagnant-lid regime.

167 In most cases, we assumed homogeneous heating, *i.e.*, H is constant throughout the
 168 system. Tidal dissipation within icy bodies may however depends on viscosity (Tobie et al.,
 169 2005), which, in our simulations, varies with temperature. We therefore calculated a few cases
 170 with viscosity-dependent internal heating. Following Roberts and Nimmo (2008), we assumed
 171 that internal heating is given by

$$172 \quad H = H_0 \left[\frac{\omega\eta/\mu}{1+(\omega\eta/\mu)^2} \right] / \left[\frac{\omega\eta_{ref}/\mu}{1+(\omega\eta_{ref}/\mu)^2} \right] \quad (8)$$

173 where η_{ref} and μ are the reference viscosity and rigidity of ice, H_0 a constant, and ω the orbital
 174 frequency. Note that the reference viscosity in Eq. (8) may be different from that defined in Eq.
 175 (6), provided that in calculations a correction is applied for consistency. Here, because we
 176 assumed that the strongest dissipation occurs close to the melting point of ice, η_{ref} is defined at
 177 the bottom of the ice shell (*i.e.*, for $\tilde{T} = 1$). In Eq. (6), by contrast, the reference viscosity η_0 is
 178 the surface viscosity (for $\tilde{T} = 0$), which implies $\eta_{ref} = \eta_0 \exp(-a_\eta)$. The non-dimensional
 179 internal heating rate may then be written

$$180 \quad \tilde{H} = \tilde{H}_0 \left[\frac{\zeta_{ref}\tilde{\eta}\exp(a_\eta)}{1+(\zeta_{ref}\tilde{\eta}\exp(a_\eta))^2} \right] / \left[\frac{\zeta_{ref}}{1+\zeta_{ref}^2} \right] \quad (9)$$

181 where $\zeta_{ref} = \omega\eta_{ref}/\mu$ and $\tilde{\eta}$ is given by Eq. (7). The viscosity at which dissipation is maximal
 182 depends on the exact value of ζ_{ref} . With μ around 4.0×10^9 Pa, orbital period of a few hours to a
 183 few days (corresponding to ω in the range 3.0×10^{-5} - 3.0×10^{-6} s $^{-1}$), and $5.0 \times 10^{12} \leq \eta_{ref} \leq 5.0 \times 10^{14}$
 184 Pas, ζ_{ref} may be chosen in the range 4.0×10^{-3} -4.0. Here, we fixed ζ_{ref} to 1, so that the maximum
 185 dissipation occurs exactly at η_{ref} . This further implies that dissipation is strongest in hottest
 186 regions, including plumes heads, as done in Tobie et al. (2003).

187 Because in our simulations viscosity varies throughout the system, the definition of the
188 Rayleigh number, Ra (Eq. 5), is ambiguous. The input Ra can however be defined at a specific
189 viscosity (or equivalently, a specific temperature), such that it does not vary during the
190 simulations. Here, we prescribed the surface Rayleigh number, Ra_{surf} , defined from the surface
191 viscosity and temperature. In stagnant-lid convection, a better description of the vigor of
192 convection beneath the lid is given by the effective Rayleigh number, Ra_{eff} , calculated with the
193 viscosity at the temperature of the well-mixed interior (or interior temperature), \tilde{T}_m , which is
194 defined as the volume averaged temperature within the adiabatic region. Following Eqs. (6) and
195 (8), Ra_{eff} is given by

$$196 \quad Ra_{eff} = Ra_{surf} \exp(a_\eta \tilde{T}_m) . \quad (10)$$

197 Note that \tilde{T}_m , and thus Ra_{eff} , are outputs of the simulations.

198 A key output observable is the amount of heat transported to the surface, measured with
199 the heat flux. In mixed-heated systems, the conservation of energy implies that its top and
200 bottom values, Φ_{top} and Φ_{bot} , satisfy

$$201 \quad \Phi_{top} = f^2 \Phi_{bot} + \frac{(1+f+f^2)}{3} H , \quad (11)$$

202 where f is the ratio between the inner and outer shell radii, equal to 1 in Cartesian geometry.
203 The characteristic heat flux is defined as the conductive heat flux for pure basal heating in
204 Cartesian geometry, $\Phi_{carac} = k \Delta T / D$, such that the non-dimensional form of Eq. (11) is
205 simply obtained by replacing each variable by its non-dimensional equivalent, $\tilde{\Phi}_{top}$, $\tilde{\Phi}_{bot}$ and
206 \tilde{H} . Equation (11) indicates that, for a given Φ_{top} , the production of heat within the system lowers
207 the amount of heat that can be extracted from regions located below (for instance, planetary
208 cores). If internal heating is too large, the system cannot extract heat from the bottom but cools
209 down both from its top and its bottom (*e.g.*, Moore 2008; Vilella and Deschamps, 2018),
210 meaning that Φ_{bot} is negative. It is useful to introduce the Urey ratio, measuring the ratio
211 between the internal heat production and the surface heat flux,

212
$$Ur = \frac{(1+f+f^2)}{3} \frac{H}{\Phi_{top}} . \quad (12)$$

213 Eqs. (11) and (12) imply that $Ur > 1$ if Φ_{bot} is negative, and $0 \leq Ur \leq 1$ otherwise.

214 Convection operates only if the convective heat flux is larger than the conductive heat
 215 flux Φ_{cond} , which, for a mixed heated system, depends on depth (Table S1). Its surface
 216 expression is given by

217
$$\Phi_{cond,top} = f \frac{k\Delta T}{D} + (f + 2) \frac{\rho HD}{6} , \quad (13)$$

218 whose non-dimensional form (with respect to the characteristic heat flux) writes

219
$$\tilde{\Phi}_{cond,top} = f + \frac{(f+2)}{6} \tilde{H} . \quad (14)$$

220 The efficiency of heat transfer is measured with the Nusselt number, Nu , defined as the ratio
 221 between the convective and conductive heat flux. Convection operates if $Nu > 1$. As an example,
 222 in Cartesian geometry ($f = 1$), $Nu > 1$ requires that the surface non-dimensional convective heat
 223 flux, $\tilde{\Phi}_{top}$, is larger than $(1 + \tilde{H}/2)$.

224 Using this setup, we performed 63 simulations in 3D-Cartesian geometry (including 9
 225 cases with heterogeneous heating) and 25 in 3D-spherical geometry (Table 1). For comparison,
 226 we also listed 5 cases with pure bottom heating taken from Deschamps and Lin (2014). Surface
 227 Rayleigh number, top-to-bottom viscosity ratio, and non-dimensional heating rate are taken in
 228 the ranges $1 \leq Ra_{surf} \leq 180$, $10^4 \leq \Delta\eta \leq 10^8$, and $0.5 \leq \tilde{H} \leq 10$ respectively, leading to effective
 229 Rayleigh numbers between 2.0×10^5 and 2.0×10^8 . In 3D-spherical cases, the inner-to-outer radii
 230 ratio is chosen between 0.6 and 0.85. For these ranges of values, the flow is time-dependent and
 231 reaches a quasi-stationary state (meaning that output properties, including \tilde{T}_m and $\tilde{\Phi}_{top}$,
 232 oscillate around constant values) after some time. Output properties are estimated after the
 233 quasi-stationary phase has been reached, by time-averaging of each property over several
 234 oscillations.

235

236 3. Flow pattern and thermal structure

237 3.1 Flow pattern

238 Stagnant-lid convection appears for top-to-bottom viscosity ratios larger than 10^4 (Moresi and
239 Solomatov, 1995), but its occurrence requires larger viscosity contrasts as the Rayleigh number
240 (Deschamps and Sotin, 2000) or shell curvature (Yao et al., 2014; Guerrero et al., 2018)
241 increases. Stein et al. (2013) proposed two criteria to assess the presence of a stagnant lid. First,
242 a non-dimensional surface velocity, \tilde{v}_{surf} , lower than 1; and second a mobility, M , defined as
243 the ratio between \tilde{v}_{surf} and the root mean square velocity of the whole system, smaller than
244 0.01. All our simulations satisfy these criteria (Table 1), and should thus belong to the stagnant-
245 lid regime.

246 Figures 1 to 3 show snapshots of temperature fields and associated horizontally averaged
247 profiles for 3D-Cartesian cases with same surface Rayleigh number ($Ra_{surf} = 25$) and viscosity
248 ratio ($\Delta\eta = 10^6$), but different rates of internal heating, and for 3D-spherical cases with $f = 0.6$,
249 $Ra_{surf} = 16$, $\Delta\eta = 10^6$ and, again, different values of \tilde{H} . A stagnant lid is clearly visible in all
250 cases. A closer examination (section 3.2) indicates that the lid is thinning with increasing \tilde{H} .
251 Internal heating has a strong impact on the flow structure beneath the lid. With increasing \tilde{H} ,
252 we observe a trend similar to that reported for isoviscous fluids (*e.g.*, Travis and Olson, 1994;
253 Deschamps et al., 2010a). Plumes are getting thinner, more diffuse and may not reach the
254 bottom of the stagnant lid, indicating that the growth of hot instabilities in the base thermal
255 boundary layer (TBL) is more difficult. The flow is progressively controlled by downwellings
256 and return flow. Importantly, if \tilde{H} is large enough (Figs. 1g-h, and 2c-d), the bottom TBL
257 disappears and the heat flux turns negative (Figure 3d and 3f). The system then cools down
258 both at its top and its bottom, and the Urey ratio (Eq. 12) is larger than 1.

259

260 3.2 Properties of the stagnant lid

261 We measured the (non-dimensional) thickness of the stagnant lid, \tilde{d}_{lid} , using the method
 262 developed by Davaille and Jaupart (1993), in which the base of the stagnant lid is defined by
 263 the intersection between the tangent at the point of inflexion of the horizontally averaged profile
 264 of vertically advected heat, $\tilde{v}_z \tilde{T}$, with the origin axis ($\tilde{v}_z \tilde{T} = 0$; left plots in Figure 3). The values
 265 of \tilde{d}_{lid} we obtained are reported in Table 1. All other parameters being equal, \tilde{d}_{lid} decreases
 266 with increasing rate of internal heating, while both \tilde{v}_{surf} and M are decreasing. Increasing
 267 internal heating thus results in thinner but stronger stagnant lids.

268 Because heat is transported by conduction in the stagnant lid, it is possible to derive
 269 analytical expressions for the horizontally averaged temperature in this region by solving the
 270 conduction heat equation. Assuming that internal heating rate and density are constant and that
 271 the surface temperature and heat flux (T_{surf} and Φ_{surf}) are known, the (dimensional) temperature
 272 profile is given either by Eq. (S7) in Cartesian geometry, or Eq. (S8) in spherical geometry of
 273 (Supporting Information, SI). Note that these expressions are independent of the lid thickness.
 274 Their non-dimensional forms are

$$275 \quad \langle \tilde{T} \rangle = \tilde{z} \tilde{\Phi}_{top} - \frac{\tilde{H}}{2} \tilde{z}^2 \quad (15)$$

276 where \tilde{z} is the non-dimensional depth, and

$$277 \quad \langle \tilde{T} \rangle = -\frac{\tilde{\Phi}_{top}}{(1-f)} \left[1 - \frac{\tilde{R}}{\tilde{r}} \right] + \frac{\tilde{H}}{6(1-f)^2} \left[2 \left(1 - \frac{\tilde{R}}{\tilde{r}} \right) + \left(1 - \frac{\tilde{r}^2}{\tilde{R}^2} \right) \right], \quad (16)$$

278 where $\tilde{r} = (1-f)^{-1} - \tilde{z}$ and $\tilde{R} = (1-f)^{-1}$ are the non-dimensional radius and total radius,
 279 respectively. Solving heat equation for viscosity-dependent internal heating is more complex in
 280 the general case. In our case, however, imposing the maximum dissipation at lowest viscosity
 281 implies that dissipation in the lid is close to zero. A good description of the temperature profile
 282 within the lid is then obtained by setting $\tilde{H} = 0$ in Eqs. (15) and (16).

283 The horizontally averaged heat flux within the stagnant lid is given by Eqs. (S11) and
 284 (S12) of SI, whose non-dimensional versions are

$$285 \quad \tilde{\Phi}(\tilde{z}) = \frac{\tilde{T}_{lid}}{\tilde{d}_{lid}} + \frac{\tilde{H}}{2} (\tilde{d}_{lid} - 2\tilde{z}) \quad (17)$$

286 and

$$287 \quad \tilde{\Phi}(\tilde{z}) = \frac{\tilde{T}_{lid}}{\tilde{d}_{lid}} f_{lid} \frac{\tilde{R}^2}{\tilde{r}^2} - \frac{\tilde{H}}{6(1-f)} \left[f_{lid}(1 + f_{lid}) \frac{\tilde{R}^2}{\tilde{r}^2} - 2 \frac{\tilde{r}}{\tilde{R}} \right], \quad (18)$$

288 where \tilde{d}_{lid} and \tilde{T}_{lid} are the non-dimensional stagnant lid thickness and basal temperature,
 289 respectively, and $f_{lid} = (R - d_{lid})/R = 1 - (1 - f) d_{lid}/D$ is the ratio between the radius of
 290 its base and the total radius. To obtain Eq. (18), it is useful to recall that $\tilde{R} = (1 - f)^{-1}$.
 291 Equations (17) and (18) can be used to estimate the temperature at the bottom of the lid as a
 292 function of the surface heat flux and stagnant lid thickness. Setting $\tilde{z} = 0$ in Eq. (17) and $\tilde{r} =$
 293 \tilde{R} in Eq. (18), and re-arranging the terms leads to

$$294 \quad \tilde{T}_{lid} = \tilde{d}_{lid} \left(\tilde{\Phi}_{top} - \frac{1}{2} \tilde{H} \tilde{d}_{lid} \right) \quad (19)$$

295 in Cartesian geometry, and

$$296 \quad \tilde{T}_{lid} = \frac{\tilde{d}_{lid}}{f_{lid}} \left[\tilde{\Phi}_{top} - \frac{1}{6} \tilde{H} \frac{(2 - f_{lid} - f_{lid}^2)}{(1-f)} \right] \quad (20)$$

297 in spherical geometry. Values of \tilde{T}_{lid} deduced either from Eq. (19) or Eq. (20) are reported in
 298 Table 1.

299 To check the validity of our approach, we inserted the values of \tilde{d}_{lid} we measured (Table
 300 1) and the values of \tilde{T}_{lid} calculated by Eqs. (19) and (20) in Eqs. (15) and (16), respectively.
 301 This provides an excellent description of the top part of the horizontally averaged temperature
 302 profiles, corresponding to the stagnant lid (dashed dark red curves in Fig. 3). Note that the
 303 values of \tilde{T}_{lid} obtained with Eq. (19) or Eq. (20) are slightly larger than that measured on the
 304 horizontally averaged profiles of temperature.

305

306 4. Scaling laws

307 Reconstructing potential thermal evolutions of planets and satellites with parameterized
308 convection methods requires the knowledge of appropriate relationships between input
309 parameters (Rayleigh number, viscosity ratio, and rate of internal heating) and observables
310 (interior temperature, surface heat flux, stagnant lid thickness), or scaling laws for short. Results
311 from our numerical simulations allow us to build such scaling laws. These are detailed below
312 and summarized in Table 2.

313

314 4.1 Temperature of the well-mixed interior

315 Numerical simulations indicate that the interior temperature of an isoviscous, mixed-heated
316 fluid is well described by a relationship combining the interior temperature for pure bottom and
317 pure internal heating (Sotin and Labrosse, 1999; Deschamps et al., 2010a). Here, we followed
318 a similar approach and built a scaling that combines the interior temperature for a bottom-heated
319 fluid animated by stagnant-lid convection (Deschamps and Lin, 2014; Yao et al., 2014), and for
320 an internally-heated fluid, leading to

$$321 \quad \tilde{T}_m = 1 - \frac{a_1}{f^{a_2\gamma}} + (c_1 + c_2 f) \left[\frac{(1+f+f^2)}{3} \tilde{H} \right]^{c_4} \frac{1}{Ra_{eff}^{c_3}}, \quad (21)$$

322 where parameters a_1 , a_2 and c_1 to c_4 can be obtained by inversion of the \tilde{T}_m predicted by
323 simulations (Table 1), and $\gamma = \Delta T / \Delta T_v$ is the non-dimensional inverse of the viscous
324 temperature scale, ΔT_v , defined as

$$325 \quad \Delta T_v = \left(-\frac{1}{\eta} \frac{d\eta}{dT} \Big|_{T=T_m} \right)^{-1}. \quad (22)$$

326 In the case of Frank-Kamenetskii approximation (Eq. 6), $\gamma = a_\eta = \ln(\Delta\eta)$. For consistency with
327 scaling laws obtained for pure bottom heating, we fixed a_1 and a_2 to the values obtained by Yao
328 et al. (2014), $a_1 = 1.23$ and $a_2 = 1.5$. We then performed two separate inversions, for $Ur < 1$ and

329 $Ur > 1$, in which we excluded simulations with heterogeneous heating. The inversion method
 330 follows the generalized inversion method of Tarantola and Valette (1982), and we assumed
 331 relative uncertainties of 0.5 % on observed \tilde{T}_m , accounting for the time-variations of this
 332 observable during the steady-state phase. For $Ur < 1$, the best fitting values are $c_1 = 4.3$, $c_2 = -$
 333 2.8 , $c_3 = 0.26$ and $c_4 = 0.96$, with a chi-square of 20 (the total number of experiments used for
 334 this inversion being 46). The value of c_3 is fairly close to the theoretical value of the Rayleigh
 335 number exponent for a purely internally heated fluid, 0.25 (Parmentier and Sotin, 2000). We
 336 therefore did an additional inversion in which we fixed c_3 to 0.25, and (for simplicity) c_4 to 1.0,
 337 and found $c_1 = 3.5 \pm 0.12$ and $c_2 = -2.3 \pm 0.11$, still with a good chi-square, around 30. We
 338 followed a similar procedure for $Ur > 1$ (28 simulations). In that case, the best fit is obtained
 339 for $c_1 = 4.5$, $c_2 = -3.1$, $c_3 = 0.34$ and $c_4 = 1.75$. Fixing, for simplicity, c_3 to 1/3, we obtained c_1
 340 $= 4.4 \pm 0.22$, $c_2 = -3.0 \pm 0.17$, and $c_4 = 1.72 \pm 0.02$, with a chi-square of 39. Figure 4a compares
 341 modelled and observed values of \tilde{T}_m . Note that the calculations with heterogeneous heating,
 342 which were all conducted with $Ur < 1$ but were not included in the inversion process, are well
 343 described by the scaling law for $Ur < 1$.

344 Because the effective Rayleigh number, Ra_{eff} , depends on \tilde{T}_m , solving Eq. (21) for \tilde{T}_m
 345 requires the use of a zero-search method. As a consequence, identifying trends in the variations
 346 of \tilde{T}_m with the input model parameters (surface Rayleigh number, rate of internal heating,
 347 thermal viscosity ratio, and curvature) is not straightforward. However, a close examination of
 348 Table 1 indicates that, other parameters being fixed, \tilde{T}_m increases with \tilde{H} and f , but decreases
 349 with Ra_{surf} . Changes of \tilde{T}_m with $\Delta\eta$ are more complex (Figure S2a). For \tilde{H} around 0.5-1.0 and
 350 higher, \tilde{T}_m first decreases with increasing $\Delta\eta$, reaches a minimum for a value of $\Delta\eta$ that
 351 increases with \tilde{H} , and then starts increasing again. For $\tilde{H} < 1$, \tilde{T}_m increases monotonically with
 352 $\Delta\eta$, as observed for purely bottom heated convection. Figures S1 and S2, built from Eq. (21)

353 further illustrate these trends. Interestingly, for the range of γ expected in ice layers, around 15-
 354 20 (section 5.1), and $\tilde{H} > 1$ one expects \tilde{T}_m to decrease with increasing viscosity ratio.

355

356 4.2 Surface heat flux

357 Heat flux through thermal boundary layers (TBL) scales as a power law of the Rayleigh number
 358 and of the temperature jump across the TBL (*e.g.*, Moore and Weiss, 1973), implying that in
 359 stagnant-lid convection it also scales as the temperature viscous scale. The horizontally
 360 averaged non-dimensional surface heat flux may then be written as a function of the Rayleigh
 361 number and of the parameter γ (section 4.1), which is, again, equal to $\ln(\Delta\eta)$ in the case of the
 362 Frank-Kamenetskii approximation. Figure 4b shows that regardless of \tilde{H} , the surface heat flux
 363 observed in our simulations with $Ur < 1$ is very well described by the scaling obtained by
 364 Deschamps and Lin (2014) and may thus be written

$$365 \quad \tilde{\Phi}_{top} = a \frac{Ra_{eff}^b}{\gamma^c}, \quad (23)$$

366 where Ra_{eff} is the effective Rayleigh number (Eq. 10), and the constants a , b , and c are equal to
 367 1.46, 0.27, and 1.21, respectively. Spherical cases for $Ur < 1$ also fit well along this
 368 parameterisation, and do not require small correction for f , as suggested by Yao et al. (2014).
 369 A reappraisal of Yao et al. (2014) calculations further shows that for $f > 0.6$ such a correction
 370 is not needed. Note that $\tilde{\Phi}_{top}$ implicitly depends on f through Ra_{eff} , which increases with
 371 interior temperature \tilde{T}_m . Because \tilde{T}_m decreases with f , $\tilde{\Phi}_{top}$ also decreases with increasing
 372 curvature. Interestingly, heat fluxes observed in cases with heterogeneous heating are slightly
 373 lower than those predicted by our scaling, but still fit very well along it, suggesting that the
 374 distribution of heat within the system does not substantially affect the surface heat flux. For Ur
 375 > 1 , our calculations indicate that $\tilde{\Phi}_{top}$ also fits well along Eq. (23) with $a = 1.57$ and values of

376 b and c similar to those for $Ur < 1$ (Figure 4b). Finally, the bottom heat flux, $\tilde{\Phi}_{bot}$, can easily
 377 be calculated by inserting Eq. (23) in the non-dimensional version of Eq. (11).

378 While increasing \tilde{H} results, of course, in larger $\tilde{\Phi}_{top}$ and smaller $\tilde{\Phi}_{bot}$, the influence of
 379 the thermal viscosity ratio, $\Delta\eta$, on $\tilde{\Phi}_{top}$ is less intuitive. The $1/\gamma^c$ term and, if γ is not too high,
 380 the decrease of \tilde{T}_m , both lower $\tilde{\Phi}_{bot}$ as $\Delta\eta$ increases. However, the exponential term in the
 381 definition of Ra_{eff} (Eq. 10) remains dominant, such that for given values of Ra_{surf} and \tilde{H} , $\tilde{\Phi}_{top}$
 382 increases with increasing $\Delta\eta$ (Figure S2). An interesting consequence is that the Urey ratio (Eq.
 383 12) decreases with increasing thermal viscosity ratio, as also shown in Table 1. In other words,
 384 given the properties (thickness, density, thermal expansion and diffusivity, super-adiabatic
 385 temperature jump, gravity acceleration, and rate of internal heating) of a mixed-heated shell
 386 animated by stagnant-lid convection, increasing viscosity ratio allows the system to extract
 387 more heat from the underlying layer (*i.e.*, the bottom heat flux increases). This somewhat
 388 counter-intuitive feature results from the strong increase in Ra_{eff} with increasing $\Delta\eta$, implying
 389 that convection in the well-mixed interior gets more vigorous.

390

391 4.3 Transition between positive and negative bottom heat flux

392 If internal heating is too large, convection cannot evacuate all the heat produced towards the
 393 surface. A fraction of this heat is released at the base of the system, resulting in a negative
 394 bottom heat flux, $\tilde{\Phi}_{bot}$. Setting $\tilde{\Phi}_{bot} = 0$ in Eq. (12) provides a criterion for the maximum
 395 amount of internal heat that can be transported to the surface as a function of the system
 396 properties (Rayleigh number, curvature, and viscosity ratio),

$$397 \quad \tilde{H}_{crit} = \frac{3a}{(1+f+f^2)\gamma^c} Ra_{eff}^b \quad (24)$$

398 Again, because Ra_{eff} depends implicitly (through \tilde{T}_m) on \tilde{H} , Eq. (24) does not have analytical
 399 solutions, but can be solved with a zero search method. An additional difficulty in estimating

400 \tilde{H}_{crit} is that, while the scalings obtained for $Ur < 1$ and $Ur > 1$ overlap at $\tilde{\Phi}_{bot} = 0$ within the
 401 error bars on scaling parameters values, they are not continuous when using the average values
 402 of these parameters (Table 2). A simple solution to this problem is to first calculate threshold
 403 values of \tilde{H} with both $Ur < 1$ and $Ur > 1$ scalings, \tilde{H}_{crit}^- and \tilde{H}_{crit}^+ , respectively, and second to
 404 define the value of \tilde{H}_{crit} as the average of these two bounds.

405 We then solved Eq. (24) for Ra_{surf} in the range 0.3-300, $\Delta\eta$ in the range 10^4 - 10^8 , and f
 406 between 1 (Cartesian geometry) and 0.6, and found that \tilde{H}_{crit} is well described by

$$407 \quad \tilde{H}_{crit} = \frac{3}{(1+f+f^2)} a_H \exp(c_H \gamma) Ra_{surf}^{b_H}, \quad (25)$$

408 where $a_H = 0.184$, $b_H = 0.31$, and $c_H = 0.19$. Equation (25) provides a convenient way to estimate
 409 \tilde{H}_{crit} and is in good agreement with our numerical simulations (Figure 5). It shows that
 410 \tilde{H}_{crit} increases with Ra_{surf} , $\Delta\eta$, and curvature (decreasing f). Note that rescaling Eq. (25) implies
 411 to multiply each of its member by $k\Delta T/\rho D^2$ (Eq. 4). Because Ra_{surf} is proportional to D^3 , one
 412 expects the dimensional critical heating rate, H_{crit} , to decrease approximately as $1/D$. Thus, the
 413 transition to a negative heat flux is reached for lower heating rates in thick layers than in thin
 414 layers, unless the thermal viscosity ratio and/or the super-adiabatic temperature jump increase
 415 dramatically with D .

416 Finally, an interesting result is that, because $\tilde{\Phi}_{bot}$ increases with the thermal viscosity
 417 ratio $\Delta\eta$ (section 4.2), \tilde{H}_{crit} also increases with $\Delta\eta$. Therefore, given the properties of a mixed-
 418 heated shell animated by stagnant-lid convection, increasing $\Delta\eta$ allows the system to extract
 419 heat from the underlying core up to higher rate of internal heating.

420

421 4.4 Thickness of the stagnant lid

422 Following Eqs. (15) and (16), the temperature profile within the lid is not a linear function of
 423 depth. However, Figure 3 suggests that these profiles are, at first order, well described by a

424 linear function. This, in turn, implies that the thickness of this lid should approximately scales
425 as the inverse of the heat flux, leading to

$$426 \quad \tilde{d}_{lid} = a_{lid} \frac{\gamma^c}{Ra_{eff}^b}, \quad (26)$$

427 where the values of parameters b and c are identical to those for surface heat flux ($b = 0.27$ and
428 $c = 1.21$), and a_{lid} is a constant. Figure 4c shows that Eq. (26) provides a good description of
429 the stagnant lid thickness, with best fit to the measured stagnant lid thicknesses obtained for a
430 value of $a_{lid} = 0.633 \pm 0.03$ for $Ur < 1$, and $a_{lid} = 0.667 \pm 0.01$ for $Ur > 1$.

431

432 5. Application to Europa

433 We now use the results obtained in section 4 to estimate the properties and thermal evolution
434 of Europa outer ice shell. Our purpose is not to provide a detailed description of Europa's
435 evolution, since we do not consider time-dependent internal heating based on Europa's orbital
436 evolution, but instead to assess quantitatively the role played by tidal heating within the ice
437 layer. This approach can easily be extended to other bodies, including Pluto, which is today
438 tidally locked but may have experienced tidal heating early in its history.

439 A feature common to many (if not all) large icy bodies of the outer solar System is the
440 persistence of a sub-surface ocean beneath an outer ice Ih shell (*e.g.*, Hussmann et al., 2007).
441 In the case of Europa the presence of a sub-surface ocean is supported by anomalies in its
442 external magnetic field, attributed to an internal magnetic field induced within a sub-surface
443 liquid layer (Khurana et al., 1998). Europa's average density suggests that its rocky core is
444 large, $\sim 70\%$ in volume, corresponding to a radius of ~ 1400 km. Given Europa's gravity
445 acceleration, 1.31 m/s^2 , the pressure at the surface of the core is not large enough to allow the
446 presence of high pressure ices. Europa's radial structure therefore likely consists of a large
447 rocky core, surrounded by a liquid layer composed of water and impurities, and an outer ice

448 layer. The exact nature of impurities is still debated. Present species may include salts, in
449 particular magnesium sulfate (MgSO_4) (Vance et al. 2018), and volatile compounds such as
450 ammonia (NH_3), methanol (CH_3OH), and methane (CH_4), which are all predicted to condensate
451 in giant planets environments with amounts up to a few per cent (*e.g.*, Mousis et al., 2009;
452 Deschamps et al., 2010b). The presence of impurities acts as an anti-freeze, opposing or
453 delaying the crystallization of the sub-surface ocean. Interestingly, while the exact nature of
454 impurities may affect the sub-surface ocean physical properties, including its density, it does
455 not qualitatively impact the crystallization process, *i.e.*, different species present in different
456 amounts would lead to similar evolution. For instance, Vilella et al. (2020) pointed out that the
457 impact of 30 % MgSO_4 on the liquidus is equivalent to that of 3.5 % NH_3 .

458 Our modelling approach is detailed in SI. It is mostly similar to the one used in
459 Deschamps (2021a), except for the treatments of the interior temperature, T_m , and of the
460 stagnant lid thickness, d_{lid} . Another important difference is that two sets of parameters are used
461 to calculate T_m and the surface heat flux, Φ_{surf} , depending on whether the bottom heat flux, Φ_{bot} ,
462 is positive ($Ur < 1$) or negative ($Ur > 1$) (Table 2). Note that instead of solving Eq. (25) to
463 decide which set of parameters to use, we apply a simpler procedure, which accounts for the
464 fact that temperature and heat flux scalings are not continuous at $Ur = 1$. First, we calculate T_m
465 and Φ_{surf} assuming parameter values for $Ur < 1$. If the corresponding Φ_{bot} calculated with Eq.
466 (11) is negative, we calculate T_m and Φ_{surf} again, but with parameter values for $Ur > 1$. If the
467 resulting Φ_{bot} turns back to positive, we set arbitrarily its value to zero and recalculate Φ_{surf} and
468 T_m accordingly.

469 Physical properties of Europa and ice Ih used for calculations are listed in Table 3, and
470 we considered two possible initial compositions for the subsurface ocean, pure water and a mix
471 of water and ammonia. In this later case, we fixed the initial amount of ammonia, $x_{\text{NH}_3}^{\text{init}}$, to 3.0
472 vol%, corresponding to about 2.2 wt%. This value may be considered as an upper (possibly

473 exaggerated) bound, and we chose it to obtain a conservative estimate of the impact of
 474 impurities on the ice shell properties and evolution. Concentration in ammonia then increases
 475 as the ice layer thickens, since only water crystalizes, while impurities are left in the sub-surface
 476 ocean. The reference viscosity, η_{ref} , is taken as a free parameter and varied between 10^{12} and
 477 10^{15} Pas, a range extended from Montagnat and Duval (2000) estimates of polar ice sheet flow.
 478 Results are presented either for a given rate of heating per mass unit, H , or a given total power
 479 dissipated in the ice shell, P_{tide} . For an ice shell thickness D_{ice} , H and P_{tide} are related by (see
 480 also Figure S3)

$$481 \quad H = \frac{3P_{\text{tide}}}{4\pi R^3 \left[1 - \left(1 - \frac{D_{\text{ice}}}{R} \right)^3 \right]}, \quad (27)$$

482 where R is the total radius of Europa.

483

484 5.1 Ice shell properties

485 As heat dissipation in the ice shell increases, two transitions may occur. First, at heating rate
 486 H_{crit} the heat flux at the bottom of the shell may turn negative, heating up the underlying sub-
 487 surface ocean and delaying its crystallization. Convection can still operate within the shell, but
 488 would be driven by downwellings and described with scaling laws for $Ur > 1$ (section 4).
 489 Second, at heating rate H_{melt} the bottom temperature exceeds the water liquidus, triggering
 490 melting at the bottom of the shell. This implies that the ice shell cannot be thicker than a critical
 491 value, D_{melt} . Local pockets of partial melt may further appear in hottest regions (plumes head),
 492 introducing additional complexities that are not accounted for by our modelling (see Vilella et
 493 al., 2020 for a discussion on this topic). Here, we estimate H_{melt} by comparing the liquidus of
 494 pure water with the ice shell horizontally averaged temperature, which underestimates the
 495 presence of local pockets of melt. However, because the inverse of the non-dimensional viscous
 496 temperature scale γ , which is here equal to $E\Delta T/RT_m^2$ (SI), is somewhat high, this bias should

497 be limited (Vilella et al., 2020). Figure 6 shows that both H_{crit} and H_{melt} decrease with increasing
 498 ice layer thickness, D_{ice} . The decrease in H_{crit} is mostly related to the thickening of the ice layer
 499 (section 4.3). The decrease in H_{melt} is a consequence of the water liquidus, which is itself
 500 decreasing with depth, thus favoring partial melting at lower heating rates. In other words, D_{melt}
 501 decreases with increasing H . Taking $H = 10^{-9}$ W/kg and a reference viscosity $\eta_{\text{ref}} = 10^{14}$ Pas,
 502 for instance, D_{melt} is around 45 km, corresponding to a total power of ~ 1.2 TW. Figure S4
 503 further indicates that all other parameters being the same, D_{melt} decreases with increasing η_{ref} .
 504 As one would expect, in the case of a pure water ocean H_{crit} is very close to H_{melt} . It is also
 505 worth noting that the addition of ammonia in the sub-surface ocean moderates the effects of H ,
 506 allowing slightly thicker ice shells at a given H .

507 Figure 7 plots the surface heat flux, interior temperature, and stagnant lid thickness as a
 508 function of the dissipated power, P_{tide} , and for different shell thicknesses. For the two ocean
 509 compositions we tested, and independently of the ice shell thickness, both T_{m} and Φ_{surf} increase
 510 with increasing P_{tide} , while the stagnant lid thins. At a given P_{tide} , thicker shells are cooler and
 511 transfer less heat, but these changes attenuate as P_{tide} increases. Interestingly, for values of P_{tide}
 512 estimated by Hussmann and Spohn (2004), in the range 0.6-1.0 TW, and despite the fact that
 513 the bottom heat flux may turn negative (in particular for cases with NH_3 in the ocean), the ice
 514 shell may be as thick as 160 km (see also Fig. 6). For slightly larger values, however, D_{melt}
 515 sharply decreases with increasing P_{tide} . In the case of a pure water ocean, for instance, it is equal
 516 to 120 and 40 km at P_{tide} of 1.1 and 1.3 TW, respectively. Finally, given D_{ice} and P_{tide} , Φ_{surf}
 517 decreases with increasing η_{ref} , while T_{m} increases and the stagnant lid thickens (Figure S5).

518

519 5.2 Thermal evolution

520 We model the ice shell thermal evolution following the approach of Grasset and Sotin (1996),
 521 solving the conservation equation of energy at the boundary between this shell and the sub-

522 surface ocean (SI). Again, a detailed reconstruction of this evolution would require to couple
523 Europa's internal and orbital evolutions (Hussmann and Spohn, 2004), implying that the tidal
524 power dissipated within the shell is time-dependent. Instead, we assumed that the dissipated
525 heat does not vary with time.

526 Examples of evolutions for $\eta_{\text{ref}} = 10^{14}$ Pas are shown in Figure S6. The ice shell first
527 thickens up to a maximum value, and then starts to thin again after a time that depends on input
528 parameters. Note that values of P_{tide} around or larger than 1.5 TW prevents the ocean
529 crystallization. The shell remains thinner than 10 km, and is not animated by convection.
530 Figures 8 and S7 plot the shell properties at time $t = 4.55$ Gyr as a function of P_{tide} and η_{ref} ,
531 respectively. As one could expect, increasing P_{tide} and/or η_{ref} reduces the final shell thickness,
532 D_{ice} , and increases its internal temperature, T_{m} . In addition, the stagnant lid thickness, d_{lid} ,
533 decreases, and convection shuts off at lower η_{ref} . Dissipated powers around or lower than 0.1
534 TW have no or small impact on D_{ice} and T_{m} , but still influences d_{lid} substantially. If η_{ref} and/or
535 P_{tide} are too small, the ocean crystallizes completely and remains frozen up to 4.55 Gyr. These
536 conclusions hold for both a pure water ocean and for an ocean with $x_{\text{NH}_3}^{\text{init}} = 3.0$ vol%. In this
537 later case, however, full crystallization cannot be completed even at low η_{ref} and/or P_{tide} .
538 Furthermore, the effects of impurities are reduced as H increases, such that the shell properties
539 get close to those for a pure water ocean. Internal heating therefore appears as a stronger
540 controlling parameter than the presence of impurities. Finally, it is worth noting that for P_{tide} in
541 the range 0.6-1.0 TW, relevant to Europa (Hussmann et al., 2004), and $\eta_{\text{ref}} = 10^{14}$ Pas, Europa's
542 ice shell should be thin, around 20-40 km at a maximum (see also Fig. S6). Lower η_{ref} allows
543 thicker shells, for instance, with $\eta_{\text{ref}} = 3.0 \times 10^{13}$ Pas, up to 120 km (pure water ocean) or 80 km
544 ($x_{\text{NH}_3}^{\text{init}} = 3.0$ vol%).

545

546 6. Conclusions and perspectives

547 The numerical simulations we performed allowed us to quantify the influence of the rate of
548 internal heating, H , on stagnant-lid convection, through the determination of scaling laws for
549 interior temperature, surface heat flux, and stagnant lid thickness (Table 2). We observed two
550 different regimes depending on the sign of the bottom heat flux, Φ_{bot} , or equivalently, whether
551 the Urey ratio is smaller or larger than 1. Interestingly, our simulations show that the value of
552 H at which Φ_{bot} turns negative increases with increasing thermal viscosity ratio, $\Delta\eta$. Another
553 interesting finding is that, while the stagnant lid stiffens with increasing H , it also thins.

554 Our simulations include a few simplifications. The rheology of ices is certainly more
555 complex than the Frank-Kamenetskii law we used. Compared to an Arrhenius-type of law, this
556 approach overestimates heat flux by up to 30 % (*e.g.*, Reese et al., 1999). In addition, different
557 mechanisms may control ice Ih deformation depending on the strain rate and/or the grain size,
558 but are not accounted for in our modelling. A full description of ice viscosity may instead
559 require the definition of a composite viscosity law, as proposed by Harel et al. (2020). Our
560 approach further neglects the possible presence of pockets of partially melted ice. Such pockets
561 may occur in plumes heads, right beneath the stagnant lid, in which case they could trigger the
562 formation of chaos and lenticulae regions (Tobie et al., 2003). Melt may also influence the
563 physical properties of ice, in particular its viscosity and density. This would in turn affect the
564 buoyancy of plumes and reduce tidal dissipation, leading to alternate phases of melting and
565 crystallization (Tobie et al., 2003). Vilella et al. (2020) further studied the impact of melt on
566 heat budget, and showed that for internal heating larger than a critical value, heat flux reaches
567 a plateau, as most of the heating is used to generate more melt. While these limitations may
568 quantitatively alter the scaling laws we build, the main trends indicated by our simulations and
569 the conclusions drawn from them should remain unchanged.

570 A full description of Europa's ice shell evolution requires coupling its orbital and thermal
571 evolutions to capture time-variations in tidal heating. By contrast, calculations coupling Io and
572 Europa evolutions suggest that tidal dissipation within Europa's ice shell may have remained
573 fairly constant around 0.6-1.0 TW during the past 4.5 Gyr (Hussmann and Spohn, 2004). If
574 true, our evolution model should provide first order, but relevant estimates of today Europa's
575 ice shell properties. Taking a reference viscosity in the range 3.0×10^{13} - 3.0×10^{14} Pas and
576 assuming the presence of impurities, the thickness of this shell should be in the range 20-75
577 km. This is larger than estimates from mechanical studies based on surface geology
578 observations (*e.g.*, Billings and Katternhorn, 2005; Dampitz and Dombard, 2011; Silber and
579 Johnson, 2017), but consistent with estimates from thermal evolution models (*e.g.*, Tobie et al.,
580 2003; Hussmann and Spohn, 2004; Allu Peddenti and McNamara, 2019; Green et al., 2021)
581 and estimates of the thickness needed to generate melts needed for cryovolcanism (Vilella et
582 al., 2020).

583 In addition to the evolution of icy bodies, our findings may have some implications for
584 the evolution of planetesimals that formed in early in solar System history. These bodies are
585 thought to have reached a few hundreds of kilometers in size and to have differentiated in a
586 core and a mantle. The decay of ^{26}Al may have released huge amounts of heat in their mantles,
587 which may, in turn, have delayed the cooling of their cores. The scaling laws we obtained can
588 be inserted in thermal evolution models of planetesimals as built, for instance, by Kaminski et
589 al. (2020). Of particular importance is the fact that, all other parameters being the same, Φ_{bot}
590 increases with increasing $\Delta\eta$ and turns negative for values of H that increase with $\Delta\eta$. This
591 suggests that, if stagnant-lid convection, triggered by large top-to-bottom temperature jump,
592 operated within the mantles of planetesimals, large amounts of heat released by the decay of
593 ^{26}Al may have helped, rather than prevented, the cooling of planetesimals cores, and possibly
594 the generation of magnetic fields within these cores.

595

596 Acknowledgments

597 The research presented in this article was supported by the National Science Council of Taiwan
598 (MoST) under grants 108-2116-M-001-017 and 107-2116-M-001-029 (FD), and JSPS
599 KAKENHI Grant JP19F19023 (KV). The data used for generating the figures displayed in this
600 article are available for academic purposes on Academia Sinica institutional repository
601 (Deschamps, 2021b). The code used in this work is not publicly available but was thoroughly
602 described in Tackley (2008).

603

604 References

- 605 Allu Peddinti, D., & McNamara, A. K. (2019). Dynamical investigation of a thickening ice-
606 shell: Implications for the icy moon Europa. *Icarus*, *329*, 251–269.
- 607 Billings, S. E., & Kattenhorn, S. A. (2005). The great thickness debate: Ice shell thickness
608 models for Europa and comparisons with estimates based on flexure at ridges. *Icarus*, *177*,
609 397–412.
- 610 Christensen, U.R. (1984). Heat transport by variable viscosity convection and implications for
611 the Earth's thermal evolution. *Phys. Earth Planet. Inter.*, *35*, 264-282.
- 612 Croft, S.K., Lunine, J.I., & Kargel, J. (1988). Equation of state of ammonia-water liquid:
613 .derivation and planetological applications. *Icarus*, *73*, 279-293.
- 614 Dampitz, A.L., & Dombard, A.J. (2001). Time-dependent flexures of the lithospheres on the
615 icy satellites of Jupiter and Saturn. *Icarus*, *216*, 86-88.
- 616 Davaille, A., & Jaupart, C. (1993). Transient high-Rayleigh-number thermal convection with
617 large viscosity variations. *J. Fluid Mech.*, *253*, 141-166.

618 Deschamps, F. (2021a). Stagnant lid convection with temperature-dependent thermal
619 conductivity and the thermal evolution of icy worlds. *Geophys. J. Int.*, 224, 1870-1890.

620 Deschamps, F. (2021b). Scaling laws for mixed-heated stagnant-lid convection and application
621 to Europa. Myspace, Academia Sinica.
622 [https://myspace.sinica.edu.tw/public.php?service=files&t=C3tVH2NGcIc1AQSYmc9GAJUce](https://myspace.sinica.edu.tw/public.php?service=files&t=C3tVH2NGcIc1AQSYmc9GAJUcebt5XxUPwhU0Tu1pJeQN8J3cySepAxRwvuUk-W6Q)
623 [bt5XxUPwhU0Tu1pJeQN8J3cySepAxRwvuUk-W6Q](https://myspace.sinica.edu.tw/public.php?service=files&t=C3tVH2NGcIc1AQSYmc9GAJUcebt5XxUPwhU0Tu1pJeQN8J3cySepAxRwvuUk-W6Q)

624 Deschamps, F., & Sotin, C. (2000). Inversion of two-dimensional numerical convection
625 experiments for a fluid with a strongly temperature-dependent viscosity. *Geophys. J. Int.*,
626 143, 204-218.

627 Deschamps, F., Tackley, P.J., & Nakagawa, T. (2010a). Temperature and heat flux scalings for
628 isoviscous thermal convection in spherical geometry. *Geophys. J. Int.*, 182, 137-154.

629 Deschamps, F., Mousis, O., Sanchez-Valle, C. & Lunine, J.I. (2010b). The role of methanol on
630 the crystallization of Titan's primordial ocean. *Astrophys. J.*, 724, 887-894.

631 Deschamps, F., & Lin, J.-R. (2014). Stagnant lid convection in 3D-Cartesian geometry: Scaling
632 laws and applications to icy moons and dwarf planets. *Phys. Earth Planet. Inter.*, 229, 40-54.

633 Grasset, O. & Sotin, C. (1996). The cooling rate of a liquid shell in Titan's interior. *Icarus*, 123,
634 101-112.

635 Green, A.P., Montesi, L.G.J., & Cooper, C.M. (2021). The growth of Europa's icy shell:
636 convection and crystallization. *J. Geophys. Res. Planets*, 126, e2020JE006677, doi:
637 10.1029/2020JE006677.

638 Guerrero, J., Lowman, J.P., Deschamps, F., & Tackley, P.J. (2018). The influence of curvature
639 on convection in a temperature-dependent viscosity fluid: implications for the 2D and 3D
640 modeling of moons. *J. Geophys. Res. Planets*, 123, 1863-1880, doi:10.1029/2017JE005497.

641 Harel, L., Dumoulin, C., Choblet, G., Tobie, G., & Besserer, J. (2020). Scaling of heat transfer
642 in stagnant lid convection for the outer ice shells of icy moons: influence of rheology. *Icarus*,
643 338, 113448, doi: 10.106/j.icarus.2019.113448.

644 Hussmann H. & Spohn, T. (2004). Thermal-orbital evolution of Io and Europa. *Icarus*, 171,
645 391-410.

646 Hussmann, H., Sotin, C. & Lunine, J.I. (2007). Interiors and evolution of icy satellites, in
647 planets and moons, *Treatise on Geophysics*, vol. 10, Elsevier, 509–539.

648 Kageyama, A., & Sato, T. (2004). “Yin-Yang grid”: an overset grid in spherical geometry.
649 *Geochem. Geophys. Geosys.*, 5, doi: 10.1029/2004GC000734.

650 Kaminski, E., Limare, A., Kenda, B., & Chaussidon, M. (2020). Early accretion of
651 planetesimals unravelled by the thermal evolution of the parent bodies of magmatic iron
652 meteorites. *Earth Planet. Sci. Lett.*, 548, 116469, doi: 10.1016/j.epsl.2020.116469.

653 Khurana, K.K., Kivelson, M.G., Stevenson, D.J., Schubert, G., Russell, C.T., Walker, R.J. &
654 Polanskey, C. (1998). Induced magnetic field as evidence for subsurface ocean in Europa and
655 Callisto. *Nature*, 395, 777-780.

656 Montagnat, M. & Duval, P. (2000). Rate controlling processes in the creep of polar ice,
657 influence of grain boundary migration associated with recrystallization. *Earth Planet. Sci.*
658 *Lett.*, 183, 179-186.

659 Moore, W.B. (2008). Heat transport in a convecting layer heated from within and below. *J.*
660 *geophys. Res.*, 113, doi:10.1029/2006JB004778.

661 Moresi, L.-N. & Solomatov, V.S. (1995). Numerical investigation of 2D convection with
662 extremely large viscosity variations. *Phys. Fluids*, 7, 2154-2162.

663 Mousis, O., Lunine, J. I., Thomas, C., Pasek, M., Marboeuf, U., Alibert, Y., Ballenegger, V.,
664 Cordier, D., Ellinger, Y., Pausat, F., & Picaud, S. (2009). Clathration of volatiles in the Solar

665 nebula and implications for the origin of Titan's atmosphere. *The Astrophysical Journal*, *691*,
666 1780-1786.

667 Roberts, J. H., & Nimmo, F. (2008). Tidal heating and the long-term stability of a subsurface
668 ocean on Enceladus. *Icarus*, *194*, 675–689.

669 Silber, E. A., & Johnson, B. C. (2017). Impact crater morphology and the structure of Europa's
670 ice shell. *Journal of Geophysical Research Planets*, *122*, 2685–2701.

671 Stein, C., Lowman, J.P., & Hansen, U. (2013). The influence of mantle internal heating on
672 lithospheric mobility: Implications for super-Earths. *Earth and Planetary Science Letters*,
673 *361*, 448–459.

674 Sotin, C., & Labrosse, S. (1999). Three-dimensional thermal convection in an iso-viscous,
675 infinite Prandtl number fluid heated from within and from below: applications to the transfer
676 of heat through planetary mantles. *Phys. Earth Planet. Inter.*, *112*, 171-190.

677 Tackley, P.J. (2008). Modelling compressible mantle convection with large viscosity contrasts
678 in a three-dimensional spherical shell using the yin-yang grid. *Phys. Earth Planet. Inter.*, *171*,
679 7-18.

680 Tarantola, A. & Valette, B. (1982). Generalized nonlinear inverse problems solved using the
681 least square criterion. *Rev. Geophys. Space Phys.*, *20*, 219-232.

682 Tobie, G., Choblet, G., & Sotin, C. (2003). Tidally heated convection: constraints on Europa's
683 ice shell thickness. *J. Geophys. Res.*, *108*, doi: 10.1029/2003JE002099.

684 Tobie, G., Mocquet, A., & Sotin, C. (2005). Tidal dissipation within large icy satellites:
685 Applications to Europa and Titan. *Icarus*, *177*, 534-549.

686 Travis, B. & Olson, P. (1994). Convection with internal sources and turbulence in the Earth's
687 mantle. *Geophys. J. Int.*, *118*, 1-19.

688 Vance, S.D., Panning, M.P., Stähler, S. & al., (2018). Geophysical investigations of habitability
689 in ice-covered ocean worlds. *J. Geophys. Res. Planets*, *123*, 180-205.

690 Vilella, K., & Deschamps, F. (2018). Temperature and heat flux scaling laws for isoviscous
691 infinite Prandtl number mixed heating convection. *Geophys. J. Int.*, 214, 265-281.

692 Vilella, K., Choblet, G., Tsao, W.E., & Deschamps, F. (2020). Tidally heated convection and
693 the occurrence of melting in icy satellites: application to Europa. *J. Geophys. Res. Planets*,
694 125, e2019JE006248, doi: 10.1029/2019JE006248.

695 Yao, C., Deschamps, F., Lowman, J.P., Sanchez-Valle, C., & Tackley, P.J. (2014). Stagnant-
696 lid convection in bottom-heated thin 3-D spherical shells: influence of curvature and
697 implications for dwarf planets and icy moons. *J. Geophys. Res. Planets*, 119, 1895-1913.

698

699
700
701
702

Tables

Table 1. Simulations of stagnant-lid convection with mixed heating.

Ra_{surf}	f	$\Delta\eta$	\tilde{H}	\tilde{H}_0	Grid size	\tilde{T}_m	$\tilde{\Phi}_{top}$	$\tilde{\Phi}_{bot}$	Ur	$rms(\tilde{v})$	\tilde{v}_{surf}	Ra_{eff}	\tilde{d}_{lid}	\tilde{T}_{lid}
<i>3D-Cartesian</i>														
16.0	-	10^4	4.0		128×128×64	1.075	3.458	-0.543	1.16	26.9	1.2×10^{-1}	3.19×10^5	0.316	0.892
32.0	-	10^4	2.0		128×128×64	0.969	2.836	0.837	0.71	40.6	3.8×10^{-1}	2.40×10^5	0.324	0.814
32.0	-	10^4	3.0		128×128×64	1.016	3.222	0.223	0.93	39.9	2.9×10^{-1}	3.71×10^5	0.302	0.835
32.0	-	10^4	4.0		128×128×64	1.051	3.678	-0.323	1.09	41.3	2.2×10^{-1}	5.12×10^5	0.280	0.872
75.0	-	10^4	1.5		128×128×64	0.937	3.202	1.702	0.47	76.9	1.01	4.21×10^5	0.268	0.804
75.0	-	10^4	3.0		128×128×64	0.998	3.668	0.670	0.82	69.7	5.4×10^{-1}	7.36×10^5	0.249	0.820
75.0	-	10^4	5.0		256×256×128	1.059	4.577	-0.422	1.09	73.4	2.5×10^{-1}	1.05×10^6	0.221	0.889
17.9	-	3.2×10^4	2.0		128×128×64	0.977	2.887	0.887	0.69	52.1	1.3×10^{-1}	4.51×10^5	0.323	0.828
17.9	-	3.2×10^4	4.0		128×128×64	1.042	3.740	-0.260	1.07	53.5	8.2×10^{-2}	8.85×10^5	0.276	0.880
55.9	-	3.2×10^4	0.0		128×128×64	0.874	3.000	3.001	0.00	112.5	7.1×10^{-1}	4.84×10^5	0.254	0.762
55.9	-	3.2×10^4	1.0		128×128×64	0.922	3.374	2.376	0.30	120.7	5.6×10^{-1}	7.92×10^5	0.252	0.818
55.9	-	3.2×10^4	2.0		256×256×128	0.962	3.649	1.649	0.55	117.4	2.6×10^{-1}	1.21×10^6	0.249	0.847
55.9	-	3.2×10^4	3.0		256×256×128	0.990	3.959	0.959	0.76	104.8	2.0×10^{-1}	1.62×10^6	0.233	0.840
55.9	-	3.2×10^4	6.0		256×256×128	1.069	5.352	-0.648	1.12	116.2	1.3×10^{-2}	3.65×10^6	0.192	0.917
178.9	-	3.2×10^4	4.0		256×256×128	0.985	5.344	1.343	0.75	198.9	5.4×10^{-1}	4.92×10^6	0.168	0.843
10.0	-	10^5	2.0		128×128×64	0.975	2.976	0.977	0.67	69.7	5.7×10^{-1}	7.62×10^5	0.319	0.849
10.0	-	10^5	4.0		256×256×128	1.034	3.818	-0.181	1.05	69.1	4.1×10^{-2}	1.38×10^6	0.273	0.894
10.0	-	10^5	6.0		256×256×128	1.110	5.007	-0.994	1.20	96.4	2.4×10^{-1}	3.60×10^6	0.224	0.971
31.6	-	10^5	0.0		256×256×128	0.891	3.143	3.144	0.00	148.1	3.0×10^{-1}	9.06×10^5	0.257	0.809
31.6	-	10^5	0.492	1.0	256×256×128	0.915	3.276	2.785	0.15	156.4	2.4×10^{-1}	1.18×10^6	0.257	0.842
31.6	-	10^5	2.0		256×256×128	0.964	3.772	1.774	0.53	148.2	1.2×10^{-1}	2.08×10^6	0.244	0.860
31.6	-	10^5	2.096	3.0	256×256×128	0.982	3.493	1.397	0.60	132.2	7.2×10^{-2}	2.57×10^6	0.246	0.858
31.6	-	10^5	4.0		256×256×128	1.006	4.471	0.471	0.89	132.6	7.3×10^{-2}	3.38×10^6	0.214	0.866
31.6	-	10^5	5.0		256×256×128	1.028	4.898	-0.101	1.02	133.7	7.2×10^{-2}	4.35×10^6	0.202	0.889
31.6	-	10^5	6.0		256×256×128	1.054	5.447	-0.553	1.10	145.7	6.6×10^{-2}	5.88×10^6	0.187	0.915
50.6	-	10^5	2.0		256×256×128	0.957	4.236	2.236	0.47	195.8	1.5×10^{-1}	3.08×10^6	0.214	0.861
50.6	-	10^5	3.0		256×256×128	0.979	4.501	1.502	0.67	169.1	1.3×10^{-1}	3.97×10^6	0.201	0.843
50.6	-	10^5	3.022	4.0	256×256×128	0.991	4.182	1.159	0.72	170.4	8.9×10^{-2}	4.58×10^6	0.206	0.860
50.6	-	10^5	6.0		256×256×128	1.035	5.710	-0.290	1.05	179.8	1.1×10^{-1}	7.60×10^6	0.174	0.900

703
704

Table 1 (*continued*).

Ra_{surf}	f	$\Delta\eta$	\tilde{H}	\tilde{H}_0	Grid size	\tilde{T}_m	$\tilde{\Phi}_{top}$	$\tilde{\Phi}_{bot}$	Ur	$rms(\tilde{v})$	\tilde{v}_{surf}	Ra_{eff}	\tilde{d}_{lid}	\tilde{T}_{lid}
50.6	-	10^5	8.0		256×256×128	1.089	6.970	-1.029	1.15	226.5	7.9×10^{-2}	1.41×10^7	0.149	0.952
50.6	-	10^5	10.0		256×256×128	1.145	8.427	-1.573	1.19	313.9	6.7×10^{-2}	2.70×10^7	0.129	1.007
56.6	-	3.2×10^5	4.0		256×256×128	0.980	5.685	1.685	0.70	326.6	9.4×10^{-2}	1.41×10^7	0.161	0.864
56.6	-	3.2×10^5	8.0		256×256×128	1.040	7.461	-0.539	1.07	354.8	7.4×10^{-2}	2.99×10^7	0.132	0.914
113.1	-	3.2×10^5	4.0		256×256×128	0.970	6.600	2.602	0.61	486.3	2.3×10^{-1}	2.48×10^7	0.137	0.867
10.0	-	10^6	1.0		256×256×128	0.940	3.913	2.914	0.31	266.4	4.0×10^{-2}	4.38×10^6	0.232	0.880
10.0	-	10^6	2.0		256×256×128	0.963	4.162	2.164	0.48	240.1	2.7×10^{-2}	5.97×10^6	0.227	0.894
10.0	-	10^6	3.0		256×256×128	0.981	4.455	1.456	0.67	213.7	2.1×10^{-2}	7.74×10^6	0.209	0.865
10.0	-	10^6	4.0		256×256×128	0.995	4.755	0.754	0.84	216.69	1.5×10^{-2}	9.33×10^6	0.203	0.882
10.0	-	10^6	4.251	5.5	256×256×128	1.012	4.442	0.192	0.96	216.81	1.7×10^{-2}	1.18×10^7	0.205	0.912
10.0	-	10^6	5.0		256×256×128	1.010	5.179	0.178	0.97	217.0	1.8×10^{-1}	1.15×10^7	0.190	0.895
10.0	-	10^6	6.0		256×256×128	1.030	5.689	-0.312	1.05	227.3	1.5×10^{-1}	1.51×10^7	0.177	0.915
10.0	-	10^6	8.0		256×256×128	1.082	7.007	-0.994	1.14	308.3	1.4×10^{-1}	3.11×10^7	0.150	0.963
25.0	-	10^6	0.0		256×256×128	0.912	4.415	4.416	0.00	456.1	2.8×10^{-1}	7.38×10^6	0.193	0.850
25.0	-	10^6	2.0		256×256×128	0.952	5.234	3.235	0.38	371.5	3.8×10^{-2}	1.29×10^7	0.171	0.868
25.0	-	10^6	2.059	3.0	256×256×128	0.959	4.984	2.926	0.41	370.8	4.5×10^{-2}	1.42×10^7	0.179	0.892
25.0	-	10^6	3.0		256×256×128	0.969	5.426	2.428	0.55	367.6	2.2×10^{-2}	1.63×10^7	0.169	0.873
25.0	-	10^6	3.041	4.0	256×256×128	0.977	5.059	2.016	0.60	355.2	3.3×10^{-2}	1.82×10^7	0.176	0.892
25.0	-	10^6	4.0		256×256×128	0.981	5.639	1.637	0.71	361.3	4.3×10^{-2}	1.92×10^7	0.165	0.876
25.0	-	10^6	4.929	6.0	256×256×128	1.001	5.564	0.635	0.89	361.2	4.6×10^{-2}	2.54×10^7	0.163	0.905
25.0	-	10^6	6.0		256×256×128	1.006	6.392	0.394	0.94	366.8	3.6×10^{-2}	2.71×10^7	0.150	0.889
25.0	-	10^6	8.0		256×256×128	1.037	7.450	-0.550	1.07	403.1	3.3×10^{-2}	4.14×10^7	0.133	0.922
45.0	-	10^6	4.0		256×256×128	0.973	6.377	2.380	0.63	515.9	8.5×10^{-2}	3.10×10^7	0.144	0.875
5.6	-	3.2×10^6	4.0		256×256×128	0.992	4.957	0.956	0.81	281.6	1.1×10^{-1}	1.57×10^7	0.194	0.886
5.6	-	3.2×10^6	8.0		256×256×128	1.065	7.130	-0.870	1.12	377.2	7.4×10^{-2}	4.71×10^7	0.146	0.958
41.9	-	3.2×10^6	4.0		256×256×128	0.967	7.495	3.496	0.53	937.6	5.4×10^{-2}	8.18×10^7	0.123	0.892
10.0	-	10^7	0.0		256×256×128	0.923	5.271	5.278	0.00	964.4	8.9×10^{-2}	2.94×10^7	0.165	0.869
10.0	-	10^7	2.948	4.0	256×256×128	0.969	6.089	3.142	0.48	753.1	1.9×10^{-2}	6.14×10^7	0.152	0.926
10.0	-	10^7	4.0		256×256×128	0.975	6.568	2.571	0.61	732.8	1.5×10^{-2}	6.76×10^7	0.149	0.935
10.0	-	10^7	8.0		384×384×192	0.940	8.115	0.114	0.99	734.9	1.1×10^{-2}	1.15×10^8	0.121	0.920
10.0	-	10^7	10.0		384×384×192	1.035	9.325	-0.676	1.07	851.5	1.0×10^{-2}	1.79×10^8	0.108	0.948
3.2	-	10^8	0.0		384×384×192	0.934	6.000	5.999	0.00	1228.2	2.0×10^{-2}	9.46×10^7	0.147	0.885
3.2	-	10^8	2.871	4.0	384×384×192	0.967	6.857	3.986	0.42	1353.7	4.8×10^{-3}	1.74×10^8	0.137	0.941
3.2	-	10^8	4.0		384×384×192	0.971	7.403	3.401	0.54	1328.9	4.0×10^{-3}	1.88×10^8	0.127	0.909

707 **Table 1** (*continued*).

Ra_{surf}	f	$\Delta\eta$	\tilde{H}	\tilde{H}_0	Grid size	\tilde{T}_m	$\tilde{\Phi}_{\text{top}}$	$\tilde{\Phi}_{\text{bot}}$	Ur	$rms(\tilde{v})$	\tilde{v}_{surf}	Ra_{eff}	\tilde{d}_{lid}	\tilde{T}_{lid}
<i>Spherical</i>														
16.0	0.60	10^6	4.0		192×576×96×2	0.932	3.970	3.767	0.67	242.7	8.0×10^{-2}	6.25×10^6	0.221	0.859
16.0	0.60	10^6	10.0		192×576×128×2	1.034	6.313	-0.607	1.03	307.6	2.2×10^{-2}	2.55×10^7	0.155	0.918
5.1	0.60	10^7	4.0		192×576×128×2	0.929	4.389	4.928	0.60	396.0	2.1×10^{-2}	1.64×10^7	0.204	0.887
10.0	0.70	10^6	8.0		192×576×96×2	0.964	3.964	2.129	0.74	193.4	3.5×10^{-2}	6.12×10^6	0.228	0.861
10.0	0.70	10^6	8.0		256×768×128×2	1.035	5.596	-0.498	1.04	234.5	1.7×10^{-2}	1.61×10^7	0.177	0.918
3.2	0.70	10^7	8.0		256×768×128×2	1.011	5.833	-0.011	1.00	366.1	4.4×10^{-2}	3.78×10^7	0.167	0.908
10.0	0.70	10^7	2.0		192×576×128×2	0.907	4.914	7.046	0.30	622.9	6.1×10^{-2}	2.23×10^7	0.171	0.854
15.8	0.70	10^7	3.0		192×576×128×2	0.917	5.845	7.461	0.37	797.0	5.8×10^{-2}	4.15×10^7	0.149	0.879
3.2	0.75	10^7	4.0		256×768×128×2	0.964	4.530	2.568	0.68	346.0	9.2×10^{-2}	1.78×10^7	0.206	0.894
3.2	0.75	10^7	8.0		256×768×128×2	1.017	6.049	-0.208	1.02	378.8	4.2×10^{-2}	4.19×10^7	0.162	0.915
3.2	0.75	10^7	10.0		256×768×128×2	1.054	7.188	-0.923	1.07	496.3	3.5×10^{-2}	7.49×10^7	0.141	0.950
10.0	0.75	10^7	4.0		256×768×128×2	0.945	5.834	4.883	0.53	660.7	2.0×10^{-2}	4.19×10^7	0.155	0.892
10.0	0.75	10^7	10.0		384×1152×192×2	1.005	7.817	0.192	0.99	716.3	9.1×10^{-3}	1.10×10^8	0.123	0.912
10.0	0.80	10^6	2.0		256×768×96×2	0.938	3.617	3.107	0.45	223.4	7.4×10^{-2}	4.25×10^6	0.242	0.859
10.0	0.80	10^6	4.0		256×768×96×2	0.977	4.267	1.580	0.76	192.0	3.0×10^{-2}	7.18×10^6	0.213	0.857
10.0	0.80	10^6	8.0		256×768×128×2	1.051	6.039	-0.729	1.08	258.1	1.6×10^{-2}	2.02×10^7	0.168	0.931
10.0	0.80	10^6	10.0		256×768×128×2	1.098	7.289	-1.315	1.12	366.4	1.3×10^{-2}	3.89×10^7	0.144	0.978
32.0	0.80	10^6	4.0		256×768×128×2	0.952	5.412	3.368	0.60	404.7	1.7×10^{-1}	1.65×10^7	0.167	0.879
3.2	0.80	10^7	4.0		256×768×128×2	0.972	4.666	2.205	0.70	359.2	1.1×10^{-2}	2.02×10^7	0.201	0.893
3.2	0.80	10^7	8.0		256×768×128×2	1.025	6.253	-0.395	1.04	401.8	3.8×10^{-3}	4.69×10^7	0.159	0.922
3.2	0.80	10^7	10.0		256×768×128×2	1.058	7.503	-0.979	1.08	557.2	4.6×10^{-3}	7.99×10^7	0.134	0.951
1.0	0.80	10^8	4.0		512×1536×192×2	0.966	5.266	3.157	0.62	626.5	2.5×10^{-3}	5.32×10^7	0.181	0.920
3.2	0.80	10^8	3.0		512×1536×192×2	0.940	6.482	6.387	0.38	1250.1	1.1×10^{-2}	1.11×10^8	0.144	0.930
10.0	0.85	10^6	4.0		256×768×128×2	0.983	4.403	1.345	0.78	201.5	2.6×10^{-2}	7.86×10^6	0.215	0.883
10.0	0.85	10^6	8.0		256×768×128×2	1.058	6.253	-0.838	1.10	283.1	1.4×10^{-2}	2.23×10^7	0.164	0.940

708 Listed parameters are the surface Rayleigh number, Ra_{surf} , the inner-to-outer radii ratio (for spherical cases), f , the top-to-bottom thermal viscosity ratio, $\Delta\eta$, the
709 non-dimensional rate of internal heating, \tilde{H} , the constant \tilde{H}_0 (for heterogeneous internal heating cases, Eq. 9), the grid size, the average non-dimensional
710 temperature of the well-mixed interior, \tilde{T}_m , the top and bottom non-dimensional heat fluxes, $\tilde{\Phi}_{\text{top}}$ and $\tilde{\Phi}_{\text{bot}}$, the Urey ratio, Ur (Eq. 12), the root mean square
711 velocity of the whole system, $rms(\tilde{v})$, the average surface velocity, \tilde{v}_{surf} , the effective Rayleigh number, Ra_{eff} (Eq. 10), the non-dimensional thickness of the
712 stagnant lid, \tilde{d}_{lid} , calculated following the method of Davaille and Jaupart (1993), and the temperature at the base of this lid, \tilde{T}_{lid} , deduced from Eq. (19) or Eq.
713 (20) with observed values of $\tilde{\Phi}_{\text{top}}$ and \tilde{d}_{lid} . Calculations with pure bottom heating ($\tilde{H} = 0$) are taken from Deschamps and Lin (2014).
714

715
716

Table 2. Summary of scaling laws

Quantity	Expression	Parameters		
		Symbol	$Ur < 1$	$Ur > 1$
Interior temperature	$\tilde{T}_m = 1 - a_1/f^{a_2}\gamma + (c_1 + c_2f) [\tilde{H}(1 + f + f^2)/3]^{c_4} / Ra_{eff}^{c_3}$	a_1	1.23	1.23
		a_2	1.5	1.5
		c_1	3.5	4.4
		c_2	-2.3	-3.0
		c_3	0.25	1/3
		c_4	1.0	1.72
Surface heat flux	$\tilde{\Phi}_{top} = a Ra_{eff}^b / \gamma^c$	a	1.46	1.57
		b	0.27	0.27
		c	1.21	1.21
Stagnant lid thickness	$\tilde{d}_{lid} = a_{lid} \gamma^c / Ra_{eff}^b$	a_{lid}	0.633	0.667
		b	0.27	0.27
		c	1.21	1.21
Threshold internal heating	$\tilde{H}_{crit} = 3a_H \exp(c_H \gamma) Ra_{surf}^{b_H} / (1 + f + f^2)$	a_H	0.184	
		b_H	0.31	
		c_H	0.19	

717 Listed expressions are scaling laws for non-dimensional interior temperature, \tilde{T}_m , surface heat flux, $\tilde{\Phi}_{top}$, stagnant lid thickness, \tilde{d}_{lid} , and internal
718 heating at the transition between positive ($Ur < 1$) and negative ($Ur > 1$) bottom heat flux, \tilde{H}_{crit} . In these expressions, \tilde{H} is the internal heating, f
719 the ratio between inner and outer radii (equal to 1 for Cartesian geometry), Ra_{surf} the surface Rayleigh number, and Ra_{eff} the effective Rayleigh
720 number calculated at $\tilde{T} = \tilde{T}_m$, given by Eq. (10). The parameter γ , controlling the amplitude of viscosity changes with temperature, is given by
721 $\gamma = \Delta T / \Delta T_v$, where ΔT_v is the viscous temperature scale (Eq. 22). Parameter values are inferred by best fitting these expressions to the results of
722 numerical simulations listed in Table 1.
723

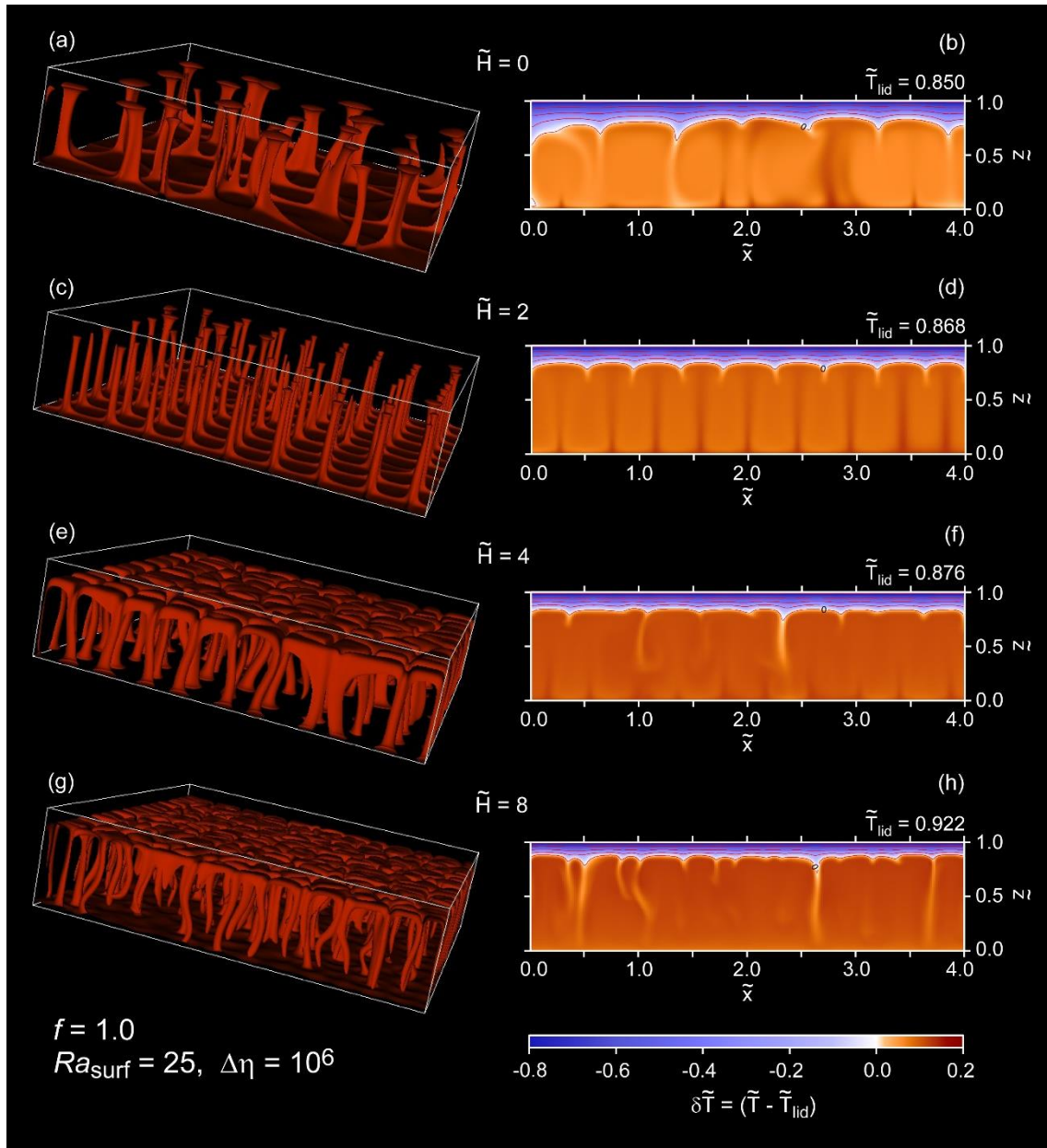
Table 3. Europa and materials properties

Parameter	Symbol	Unit	Value/Expression	Europa
<i>Ice Ih properties</i>				
Density	ρ_I	kg/m ³	920	
Thermal expansion	α_I	1/K	1.56×10^{-4}	
Thermal conductivity	k_I	W/m/K	$566.8/T$	
Heat capacity	C_p	J/kg/K	$7.037T + 185$	
Thermal diffusivity	κ_I	m ² /s	$k/\rho_I C_p$	
Latent heat of fusion	L_I	kJ/kg	284	
Reference bulk viscosity	η_{ref}	Pa s	10^{12} - 10^{15}	
Activation energy	E	kJ/mol	60	
<i>Liquid water/ammonia properties</i>				
Density (water)	ρ_w	kg/m ³	1000	
Density (ammonia)	ρ_{NH_3}	kg/m ³	734	
Thermal expansion (water)	α_w	1/K	3.0×10^{-4}	
Heat capacity (water)	C_w	J/kg/K	4180	
<i>Silicate core properties</i>				
Density	ρ_c	kg/m ³	3300	
Thermal diffusivity	κ_c	m ² /s	10^{-6}	
<i>Europa properties</i>				
Total radius	R	km		1561
Core radius	r_c	km		1400
Gravity acceleration	g	m/s ²		1.31
Surface temperature	T_{surf}	K		100
Surface thermal conductivity	k_{surf}	W/m/K		5.7

726 All data for ice Ih and liquid water properties are similar to that used by Kirk and Stevenson
727 (1987) (see references therein), except liquid ammonia density, which is from Croft et al.
728 (1988), bulk viscosity, which is a free parameter with possible range of values extended from
729 Montagnat and Duval (2000) estimates, and the activation energy, which is taken from the
730 intermediate regime of Durham et al. (2010).
731

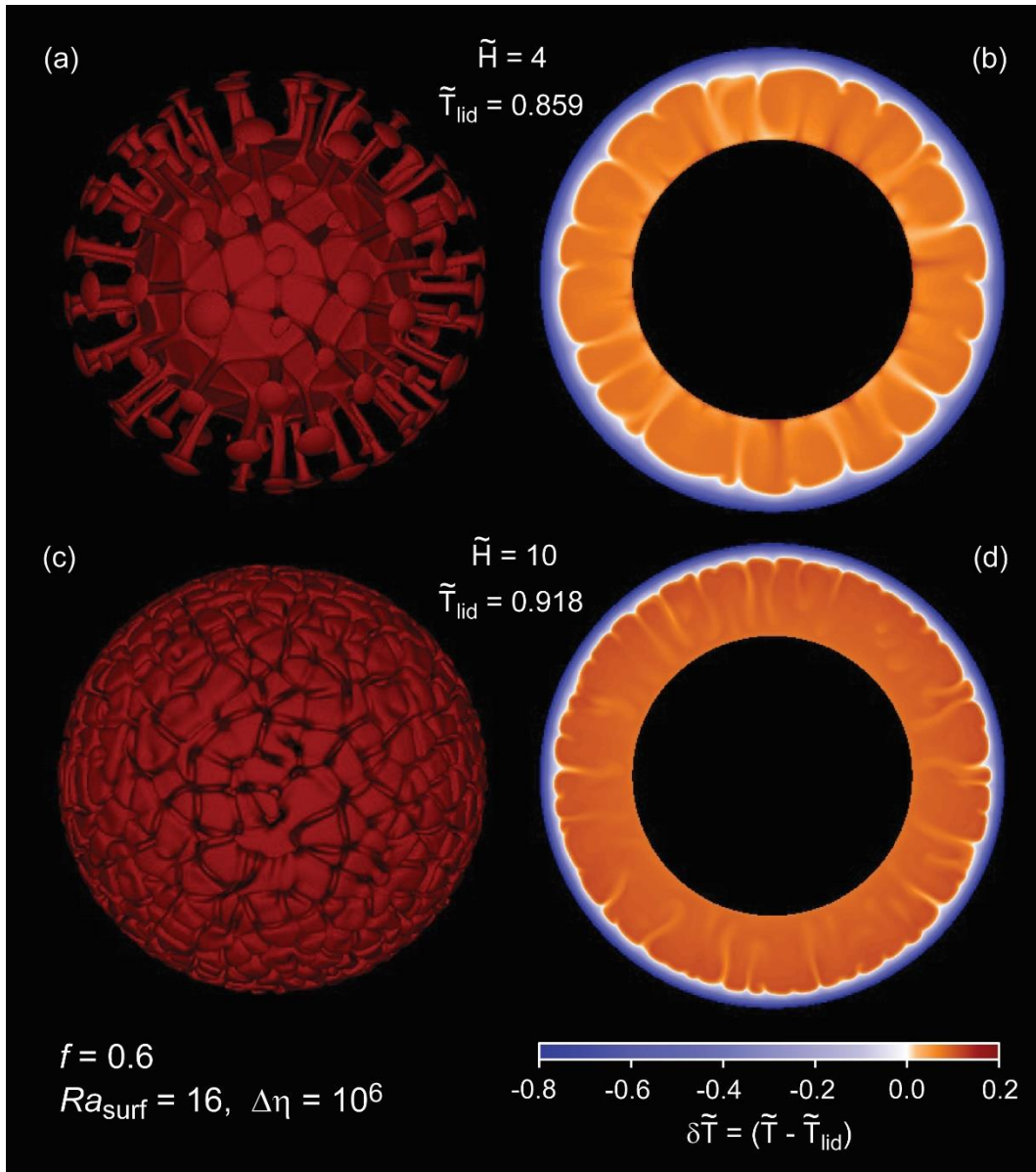
732 Figures

733
734



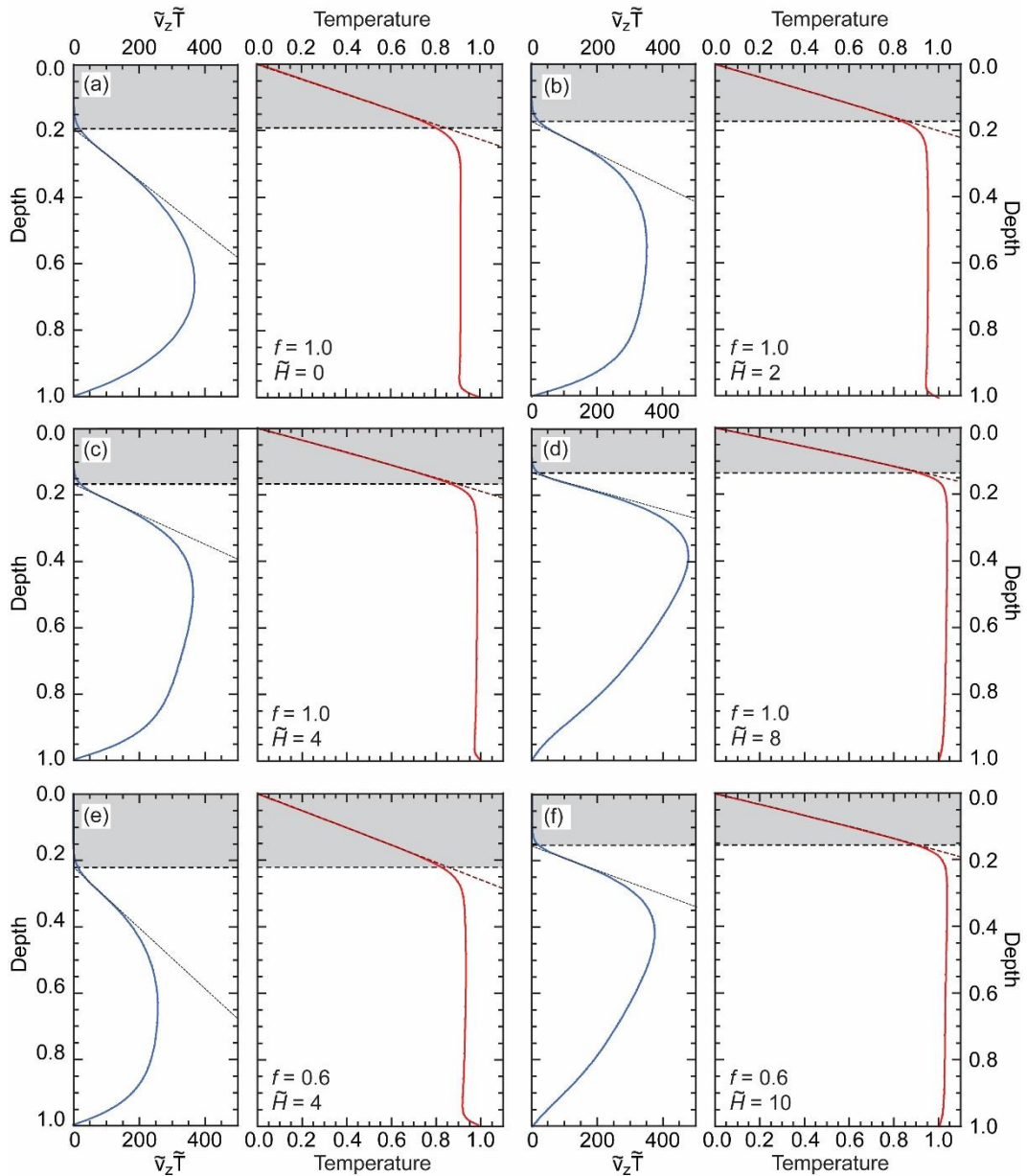
735

736 **Figure 1.** Snapshots of the temperature field (left) and vertical slices of the residual temperature
 737 relative to the temperature at the bottom of the stagnant lid \tilde{T}_{lid} (right) for cases with surface
 738 Rayleigh number $Ra_{surf} = 25$, thermal viscosity ratio $\Delta\eta = 10^6$ and different values of the non-
 739 dimensional rate of internal heating, \tilde{H} . (a-b) $\tilde{H} = 0$ (pure bottom heating), (c-d) $\tilde{H} = 2$, (e-
 740 f) $\tilde{H} = 4$, and (g-h) $\tilde{H} = 8$. Isosurface values are (a) $\tilde{T} = 0.95$, (c) $\tilde{T} = 0.97$, (e) $\tilde{T} = 0.95$,
 741 and (g) $\tilde{T} = 1.015$. In the case with $\tilde{H} = 8$ (plots g-h) the bottom heat flux is negative, *i.e.*, the
 742 system cools down both at its top and its bottom. Value of \tilde{T}_{lid} are indicated on each panel.
 743



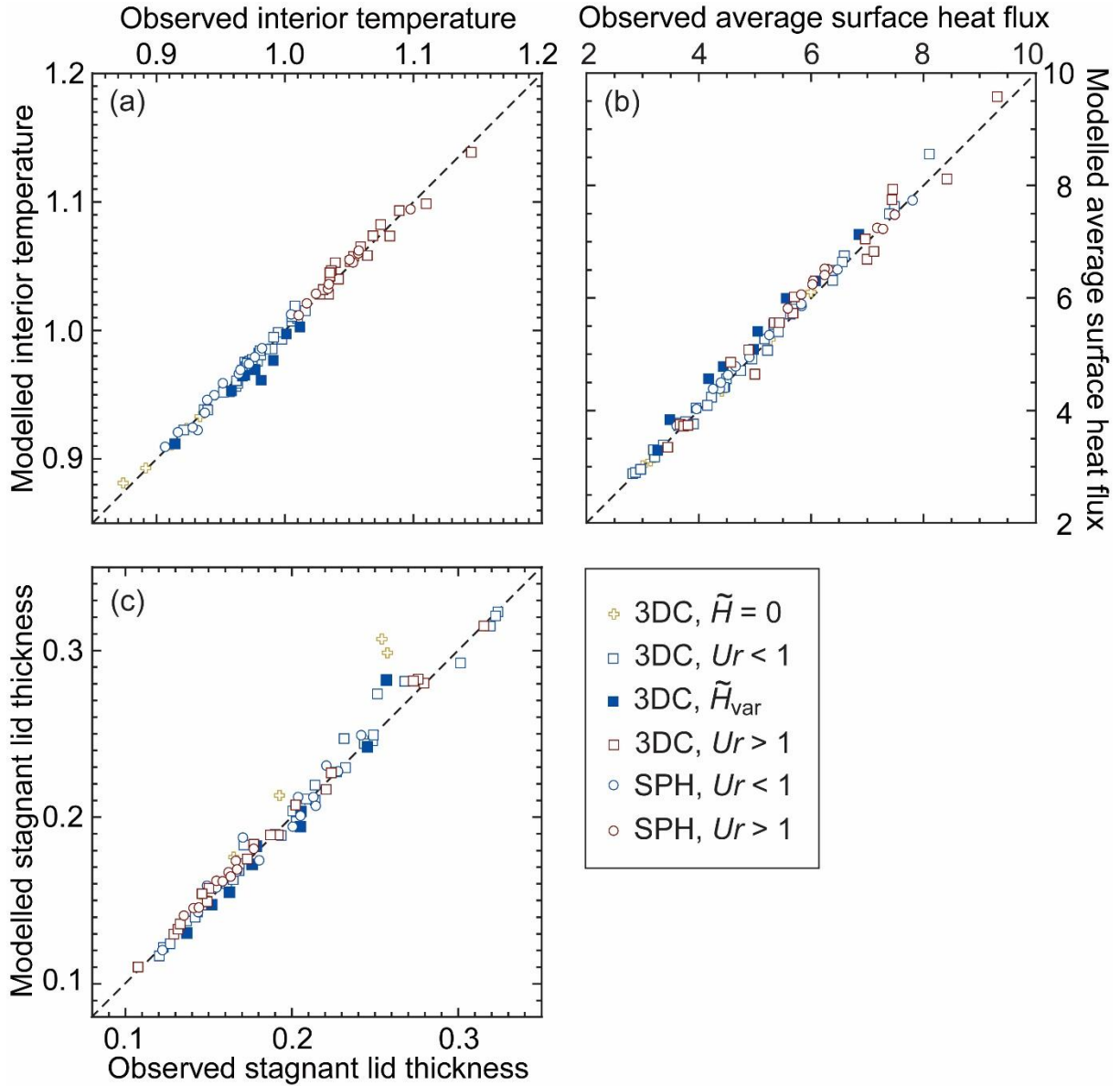
745

746 **Figure 2.** Isosurface of the temperature (left) and polar slices of the residual temperature
 747 relative to the temperature at the bottom of the stagnant lid \tilde{T}_{lid} (right) for snapshots of two
 748 cases in 3D-spherical geometry with $f = 0.6$, surface Rayleigh number $Ra_{surf} = 16$, thermal
 749 viscosity ratio $\Delta\eta = 10^6$ and two values of the non-dimensional rate of internal heating, $\tilde{H} = 4$,
 750 (a-b) and $\tilde{H} = 10$ (c-d). Isosurface values are $\tilde{T} = 0.95$ in plot (a) and $\tilde{T} = 1.03$ in plot (c). In
 751 the case with $\tilde{H} = 10$ (plots c-d), the bottom heat flux is negative, *i.e.*, the system cools down
 752 both at its top and its bottom. Value of \tilde{T}_{lid} are indicated on each panel.
 753



755

756 **Figure 3.** Horizontally averaged profiles of temperature (right plot in each panel) and vertically
 757 advected heat flow (left plot) for four cases in 3D-Cartesian geometry (plots a-d) and two cases
 758 in 3D-spherical geometry with inner-to-outer radii ratio $f = 0.6$ (plots e-f). Surface Rayleigh
 759 number, Ra_{surf} , is equal to 25 for 3D-Cartesian cases and 16 for spherical cases, and the top-to-
 760 bottom viscosity ratio is $\Delta\eta = 10^6$ in all cases. The non-dimensional heating rate is (a) $\tilde{H} = 0$,
 761 (b) $\tilde{H} = 2$, (c) $\tilde{H} = 4$, (d) $\tilde{H} = 8$, (e) $\tilde{H} = 4$, (f) $\tilde{H} = 10$. The grey areas denote the vertical
 762 extension of the stagnant lid. The dashed lines in the plots of advected heat flow show the
 763 tangent to the point of inflexion, whose intersection with the origin axis defines the bottom of
 764 the lid. The dashed dark-red curves in the plots of temperature are determined assuming a
 765 conductive temperature profile in the stagnant lid, and are calculated following either $\tilde{T}(\tilde{z}) =$
 766 $\tilde{T}_{\text{lid}} z/\tilde{d}_{\text{lid}}$ (panel a), Eq. (15) (panels b-d) or Eq. (16) (panel e-f) with values of \tilde{d}_{lid} listed in
 767 Table 1, and values of \tilde{T}_{lid} estimated from Eq. (19) or Eq. (20).
 768



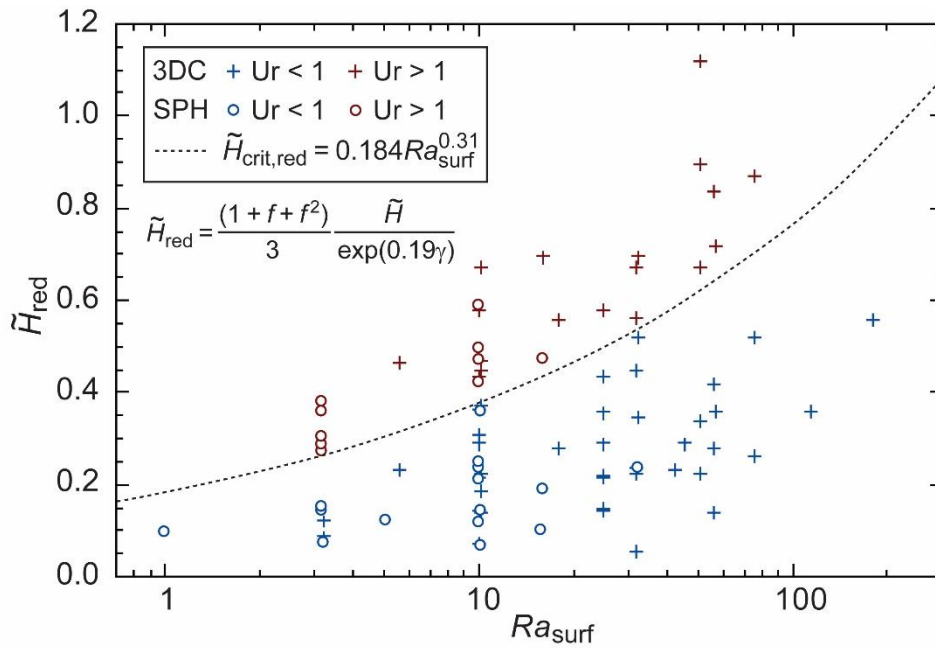
770

771 **Figure 4.** Comparison between observed and modelled output properties. (a) Temperature of
 772 the well-mixed interior, \tilde{T}_m . Observed values are listed in Table 1, and modelled values are
 773 given by Eq. (21) with parameter values discussed in section 4.1. (b) Surface heat flux, $\tilde{\Phi}_{top}$.
 774 Observed values are listed in Table 1, and modelled values are calculated by Eq. (23) with
 775 parameter values discussed in section 4.2. (c) Thickness of the stagnant lid, \tilde{d}_{lid} . Observed
 776 values are listed in Table 1, and modelled values are calculated by Eq. (26) with parameter
 777 values discussed in section 4.4.

778

779

780
781



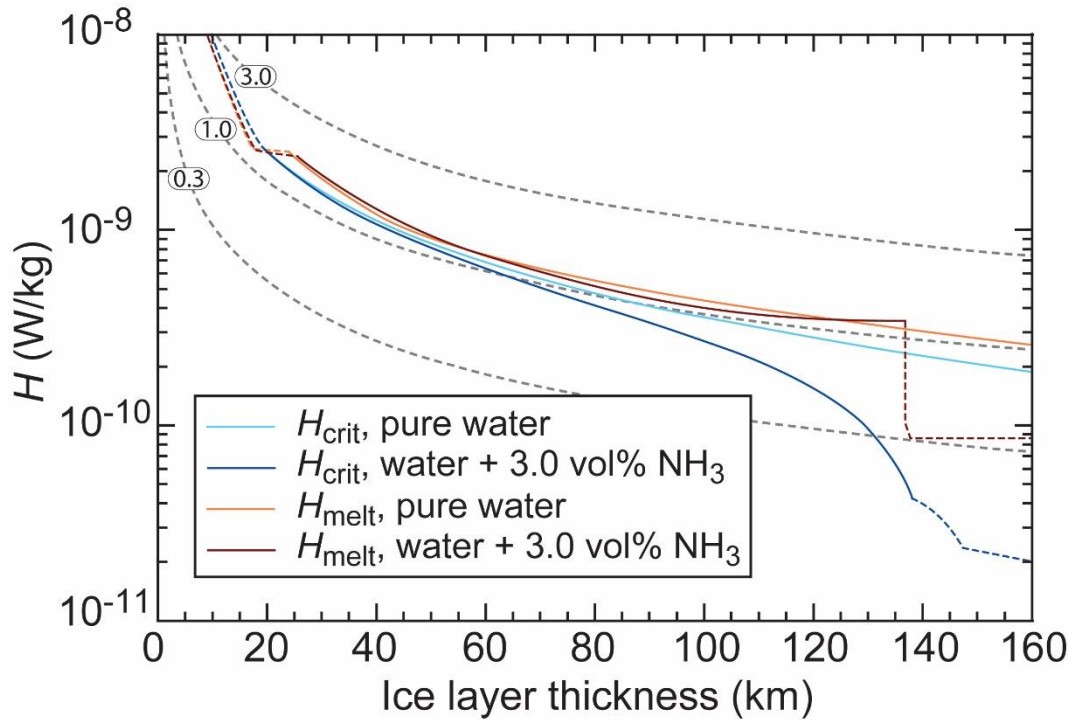
782

783 **Figure 5.** Reduced non-dimensional heating rate, $\tilde{H}_{red} = \exp(0.19\gamma) (1 + f + f^2)/3$, as a
784 function of surface Rayleigh number, Ra_{surf} . Blue and red symbols plot our numerical
785 simulations (Table 1) with positive and negative bottom heat flux, respectively, and the dashed
786 curve shows the (reduced) critical rate of internal heating for which the bottom heat flux turns
787 negative, \tilde{H}_{crit} , calculated with Eq. (25).

788

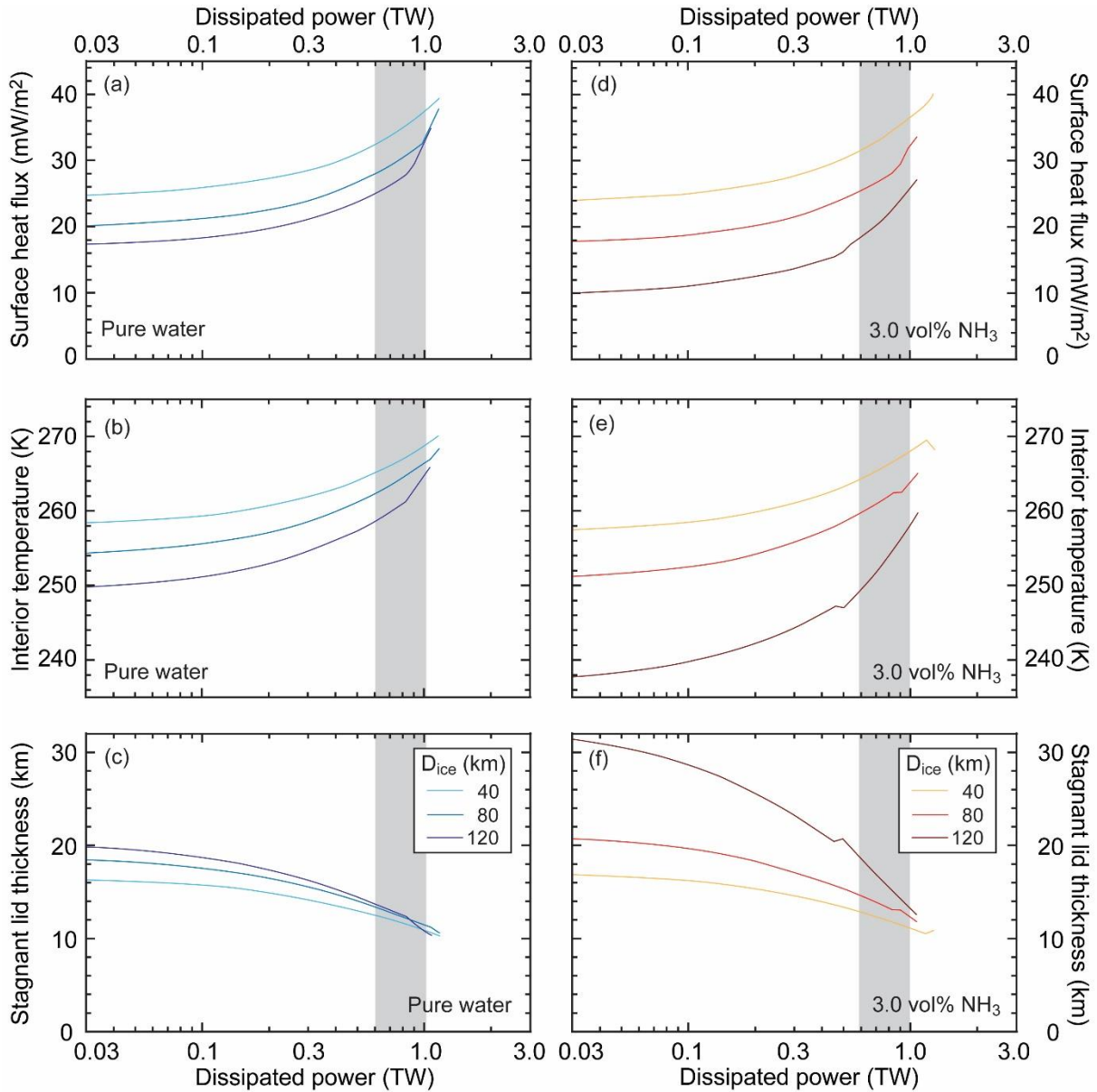
789

790
791



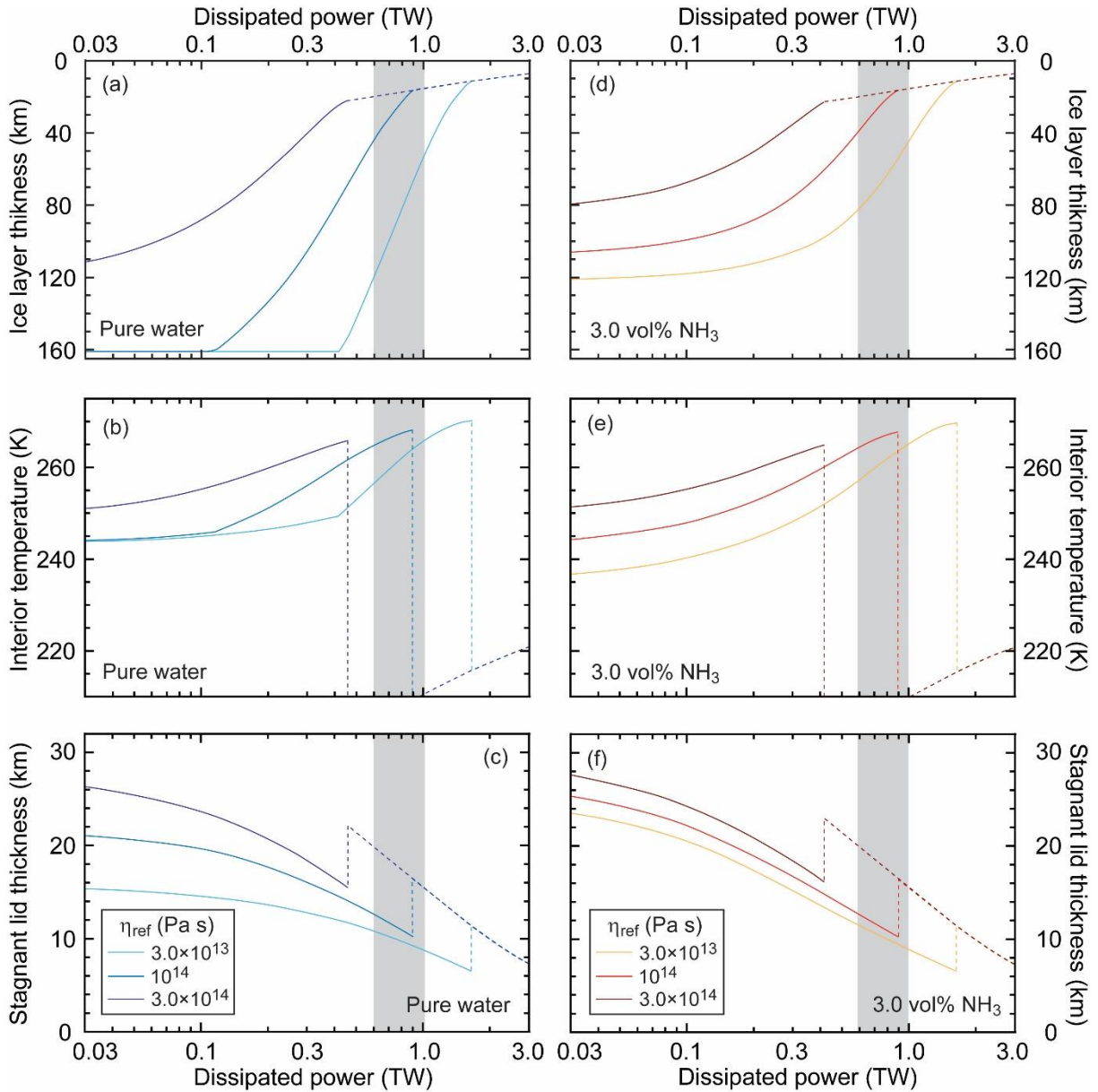
792
793
794
795
796
797
798
799
800
801
802

Figure 6. Critical values of internal heating for the transition between a positive and negative bottom heat flux, H_{crit} , and for partial melting of the ice shell, H_{melt} , as a function of the ice shell thickness. Calculations are made with the properties of Europa (Table 3), $\eta_{ref} = 10^{14}$ Pa s, and for two possible compositions of the sub-surface ocean, pure water and an initial mix (*i.e.*, for a shell thickness equal to 0) of water and 3.0 vol% ammonia. Dashed parts of the curves indicate that the system is not animated by convection, based on the observation that the convective heat flux is smaller than the corresponding conductive heat flux. The grey dashed curves represent the heating rate for three values of the total power dissipated within the ice shell (values in TW indicated on each curve).



804

805 **Figure 7.** Properties of Europa's outer ice shell as a function of the power dissipated within this
 806 shell, and for three selected shell thicknesses (color code). (a) and (d) Surface heat flux. (b) and
 807 (e) Interior temperature. (c) and (f) Stagnant lid thickness. Physical properties used for
 808 calculations are listed in Table 3, the reference viscosity η_{ref} is equal to 10^{14} Pa s, and two initial
 809 compositions of the ocean are considered, pure water (left column), and an initial mix of water
 810 and 3.0 vol% ammonia (right column). Curves interruptions indicate that the average interior
 811 temperature is larger than the liquidus of pure water at this depth. For the cases with ammonia,
 812 two regimes occur depending on whether the Urey ratio (Ur , Eq. 12) is smaller or larger than
 813 1, leading to discontinuities at $Ur \sim 1$. The grey shaded bands represent the possible range of
 814 dissipated power according to Hussman and Spohn (2004).
 815



817

818 **Figure 8.** Properties of Europa's outer ice shell at $t = 4.55$ Gyr as a function of the power
 819 dissipated within the shell and for three values of the reference viscosity, η_{ref} (color code). (a)
 820 and (d) Thickness. (b) and (e) Interior temperature. (c) and (f) Stagnant lid thickness. Physical
 821 properties used for calculations are listed in Table 3, and two initial compositions of the ocean
 822 are considered, pure water (left column), and an initial mix of water and 3.0 vol% ammonia
 823 (right column). Dashed parts of the curves indicate that the system is not animated by
 824 convection. The grey shaded bands represent the possible range of dissipated power according
 825 to Hussman and Spohn (2004).

826